Mon. Not. R. Astron. Soc. **398,** 451–470 (2009) doi:10.1111/j.1365-2966.2009.15160.x

PopStar I: evolutionary synthesis model description

M. Mollá,[1⋆] M. L. García-Vargas[2] and A. Bressan[3,4,5]

[1]*Departamento de Investigación Básica, CIEMAT, Avda. Complutense 22, 28040 Madrid, Spain*
[2]*FRACTAL SLNE, C/ Tulipán 2, p13, 1A , 28231 Las Rozas de Madrid, Spain*
[3]*INAF Osservatorio Astronomico di Padova, Viccolo dell' Osservatorio-5, 35122 Padova, Italy*
[4]*SISSA-ISAS, International School for Advanced Studies, Via Beirut 4, 34014 Trieste, Italy*
[5]*INAOE, Luis Enrique Erro 1, 72840, Tonantzintla, Puebla, Mexico*

Accepted 2009 May 29. Received 2009 April 23; in original form 2009 January 13

ABSTRACT

We present new evolutionary synthesis models for simple stellar populations for a wide range of ages and metallicities. The models are based on the Padova isochrones. The core of the spectral library is provided by the medium resolution Lejeune et al. atmosphere models. These spectra are complemented by Non Local Thermodynamic Equilibrium (NLTE) atmosphere models for hot stars that have an important impact on the stellar cluster's ionizing spectra: O, B and WR stellar spectra at the early ages, and spectra of post asymptotic giant branch stars and planetary nebulae, at intermediate and old ages. At young ages, our models compare well with other existing models, but we find that the inclusion of the nebular continuum, not considered in several other models, significantly reddens the integrated colours of very young stellar populations. This is consistent with the results of spectral synthesis codes particularly devised for the study of starburst galaxies. At intermediate and old ages, the agreement with the literature model is good and, in particular, we reproduce the observed colours of star clusters in Large Magellanic Cloud well. Given the ability to produce good integrated spectra from the far-ultraviolet to the infrared at any age, we consider that our models are particularly suited for the study of high-redshift galaxies. These models are available on the web site http://www.fractal-es.com/SEDmod.htm and also through the Virtual Observatory Tools on the PopStar server.

Key words: galaxies: abundances – galaxies: evolution – galaxies: starburst – galaxies: stellar content.

1 INTRODUCTION

Spectrophotometric evolutionary synthesis models are the basic tools to obtain information about age, metallicity, mass, star formation history and other properties of objects whose stellar populations are unresolved. Population synthesis has proven to be now even more important to analyse data obtained from large surveys or/and from high-redshift galaxies, and to extract the star formation histories of millions of galaxies (e.g. Clemens et al. 2006; Annibali et al. 2007; Asari et al. 2007; Cid Fernandes et al. 2007; Clemens et al. 2009a).

Almost all the models used to study the integrated properties of stellar systems rest now on the notion, first introduced by Tinsley (1972), that the stellar birthrate can be split into the product of a time-independent function providing the star mass distribution, the initial mass function (IMF) and a mass-independent function providing the star formation rate. In this way, the integrated properties of a galaxy can be modelled as a combination of simple stellar populations (SSP) that can be considered as the building blocks of the population synthesis technique (Bruzual 1983).

There have been in the past many studies devoted to the computation of integrated properties of SSPs, for example Bressan, Chiosi & Fagotto (1994), Bruzual & Charlot (2003, hereafter BC03), Leitherer et al. (1999, hereafter STB99), Bicker et al. (2004), González Delgado et al. (2005, hereafter GON05), Maraston (2005, hereafter MAR05) and Fritze-v. Alvensleben & Bicker (2006). Important differences between these SSP models arise from the use of different stellar tracks (or isochrones), different stellar atmosphere libraries, different spectral coverage and resolution, inclusion of nebular emission and different input physics and computational algorithms. It is also worth noting that many of the existing codes are optimized for the application to particular types of objects. For example, STARBURST99 is tuned to analyse starburst galaxies, while other standard evolutionary synthesis models are mainly suited for old stellar populations.

Particularly important today, where a large observational effort is devoted to high-redshift galaxies, is the ability to accurately describe the concomitant presence of very young- and intermediate-age (from a fraction to a few Gyr) stellar populations. Indeed, in the

⋆E-mail: mercedes.molla@ciemat.es

studies of high-redshift galaxies, it has been shown that the use of models based on different ingredients may dramatically change the estimates of ages and masses of the underlying stellar populations (MAR05; Bruzual 2007).

This piece of work is the first paper of a series of three dedicated to PopStar model description and initial test-cases application. In this paper, Paper I, we describe PopStar models and show their good calibration with previous ones. We emphasize their suitability to model stellar populations in a wide range of age and metallicity. Paper II summarizes the results of computing the emission line spectra of the H II regions ionized by the youngest star clusters and compares these results with a sample of H II regions where the metallicity has been carefully determined through appropriate calibrators. Finally, Paper III calculates the photometrical properties of young star clusters, taking into account the contamination by the emission lines in the computed colours and the underlying old populations where these clusters are embedded with the aim of being able to determine the cluster physical properties from the photometrical information only in order to apply to large photometrical surveys.

The aim of this paper is to present an updated version of our evolutionary synthesis code (García-Vargas, Mollá & Bressan 1998; Mollá & García-Vargas 2000, hereafter MGV00) that makes it suitable for the study of a wide range of stellar populations, from those extremely young to the oldest one, in a widest as possible spectral range. This is required on one side by the increasing relevance of young- and intermediate-age stellar populations in observed magnitudes and colours of high-redshift galaxies and, on the other, by the advent of multiband observations that cover at least from the rest-frame far-ultraviolet (UV) to beyond the near-infrared.

We present a new code that combines a revision of the Padova isochrones used in García-Vargas et al. (1998), mainly in the computation of intermediate-age stellar populations, with the best updated stellar model spectra, including nebular emission for the youngest ages. The SSP spectra are based on the stellar atmosphere models by Lejeune, Cuisinier & Buser (1997) and Smith, Norris & Crowther (2002a) for normal and massive stars, respectively, and the planetary nebula (PN) models by Rauch (2003). The main reason for avoiding the use of empirical libraries is that they still provide an incomplete coverage of the parameter space (effective temperature, gravity, metallicity, wavelength). The reason to avoid the use of other theoretical atmosphere libraries with good parameter space coverage and even finer spectral resolution is that the latter models have not been yet carefully tested against observations as the one we have adopted. The models presented here are thus at medium spectral resolution, and they have not been computed for comparison with high-spectral-resolution observations, like those recently published by GON05 and Coelho et al. (2007). However, there are no, at the moment, high-resolution spectra for all the stellar phases considered in this paper, and thus we paid more attention to the wide wavelength coverage, because our goal is to provide models useful for the study of high-redshift galaxies.

Finally, we remind that in the last decade the importance of considering the effects of dust was recognized, not only for the extinction but also for the re-emission of the light in the mid- and far-infrared spectral regions, with the consequent extension of the population synthesis into these new spectral windows (Bressan, Granato & Silva 1998; Bressan et al. 2006; Marigo et al. 2008; Clemens et al. 2009b) and even into the radio window (Bressan, Silva & Granato 2002). As for the majority of literature models, also those presented here do not account for this effect directly, but they can be used in existing galaxy spectral evolution codes that account for the effects of dust as, for example, GRASIL (Silva et al. 1998; Panuzzo et al. 2003; Vega et al. 2008).

The plan of this paper is as follows. In Section 2, we summarize the main characteristics of evolutionary tracks (Padova 94), isochrone calculation and stellar atmosphere models adopted. In Section 3, we illustrate and discuss the inclusion of the nebular contribution. In Section 4, we present the photometrical evolution of our SSP and compare it with that obtained by other selected models existing in the literature. Finally, our conclusions are drawn in Section 5.

2 THE EVOLUTIONARY SYNTHESIS MODEL

2.1 The stellar evolution: the isochrones

The grid is composed by SSPs for six different IMFs whose characteristics are summarized in Table 1. The Salpeter (1955) power law, $\phi(m) \propto m^{-(\alpha+1)}$ with α =1.35 with mass limits: (a) between 0.85 and 120 $M_\odot$, and (b) between 1.00 and 100 $M_\odot$, have been used for comparison with other set of models, in particular García-Vargas, Bressan & Diaz (1995) and STB99, respectively. The other IMF functions listed in Table 1 are Salpeter (1955), Ferrini, Penco & Palla (1990), Kroupa (2001) and Chabrier (2003), all of them computed with masses between 0.15 and 100 $M_\odot$. The expressions are

$$\phi(m)_{\rm SAL} = m^{-2.35}, \tag{1}$$

$$\phi(m)_{\rm FER} = 10^{-\sqrt{0.73+\log m(1.92+\log m 2.07)}}/m^{1.52}, \tag{2}$$

$$\phi(m)_{\rm KRO} = \begin{cases} m^{-0.35} & 0.15 \le m/{\rm M}_\odot < 0.08 \\ 0.08m^{-1.3} & 0.08 \le m/{\rm M}_\odot < 0.50 \\ 0.04m^{-2.3} & 0.50 \le m/{\rm M}_\odot < 100, \end{cases} \tag{3}$$

$$\phi(m)_{\rm CHA} = \begin{cases} 0.037m^{-1}{\rm e}^{-\frac{(\log m+0.658)^2}{0.65}} & 0.15 \le m/{\rm M}_\odot < 1 \\ 0.019m^{-2.3} & 1 \le m/{\rm M}_\odot \le 100 \end{cases}. \tag{4}$$

The isochrones used in this work have been computed for six different metallicities: $Z = 0.0001$, 0.0004, 0.004, 0.008, 0.02 and 0.05, adopting stellar evolutionary tracks from Bressan, Bertelli & Chiosi (1993), Fagotto et al. (1994a,b) and Girardi et al. (1996). While the general properties of the stellar evolutionary tracks can be found in the above papers, we stress here a few points that are relevant for this paper.

(i) *Mass loss*. Mass loss is an important ingredient in the context of this paper, because in old- and intermediate-age stellar populations it determines the current stellar mass on the Horizontal Branch and on the post asymptotic giant branch (P-AGB) phases, while in young populations it affects the relative distribution between supergiant and Wolf–Rayet (WR) single stars.

Table 1. Summary of the used IMFs.

IMF	$m_{\rm low}$ ($M_\odot$)	$m_{\rm up}$ ($M_\odot$)	Reference
SAL1	0.85	120	Salpeter (1955)
SAL2	0.15	100	Salpeter (1955)
FER	0.15	100	Ferrini et al. (1990)
CHA	0.15	100	Chabrier (2003)
KRO	0.15	100	Kroupa (2001)
STB	1.00	100	Salpeter (1955)

Along the red giant branch (RGB) phase of low-mass stars, mass loss is accounted for by means of the Reimers formulation, assuming $\eta_{\rm RGB} = 0.50$ independently of the metallicity as suggested by Carraro et al. (1996) and more recently by van Loon, Boyer & McDonald (2008). The AGB phase of old- and intermediate-age populations is calculated according to Bressan et al. (1998). The adopted value of $\eta_{\rm RGB}$ is slightly larger than that assumed by Bressan et al. (1998), $\eta_{\rm RGB} = 0.45$. However, with these prescriptions the isochrones reproduce the UV-integrated properties of Globular Clusters fairly well (Chavez et al. 2009), and the observed *Spitzer* Infrared Spectrograph (IRS) spectra and mid-infrared colours of ellipticals in Virgo (Bressan et al. 2006), and Coma (Clemens et al. 2009b), clusters, i.e. old stellar populations likely at the two extremes of the metallicity range of stellar systems. At intermediate ages, the colours compare well with the observations of Large Magellanic Cloud (LMC) clusters (Persson et al. 1983; Kyeong, Tseng & Byun 2003; Goudfrooij et al. 2006; Pessev et al. 2006) as shown later.

The mass-loss formulation adopted in massive stars is amply described in the relative quoted papers. Here, we remind that it was included in the computation of the evolutionary tracks with a metallicity dependence $\sqrt(Z)$, *independently from the evolutionary status*. The surface hydrogen, helium and carbon abundances are used to discriminate blue supergiant form WR stars, and to identify the main WN and WC evolutionary phases, as described in García-Vargas et al. (1995). In this respect, we remind that, besides mass loss, the appearance of the WR phase depends strongly also on other input physics like the stellar rotation (Meynet & Maeder 2005; Vázquez et al. 2007) and/or the evolution within a binary system (e.g. Vanbeveren, Van Bever & Belkus 2007) with suitable orbital parameters. These effects are not included in our treatment.

(ii) *Ages*. The age coverage is from $\log\tau$ 5.00 to 10.30 with a variable time resolution which is $\Delta(\log\tau) = 0.01$ in the youngest stellar ages. At ages of a few million years, low-mass stars are still contracting on the main sequence. This is not very important for the integrated properties because, under our IMF assumptions, the integrated luminosity is dominated by the most massive stars. At these young ages, however, the latter stars may be still embedded in their parent molecular cloud, with the consequence that their ionizing spectra may be heavily modified by extinction. The effect in these cases would be that dust may attenuate the flux of ionizing photons, changing the total intensity and hardness of the ionizing spectrum. This effect is not considered in this paper, but it will be the subject of a forthcoming investigation devoted to the effects of dust in young star-forming regions. Nevertheless, our results are applicable to many star formation regions (e.g. Giant Extragalactic H II regions) that are not dominated by dust since massive stars are clearly visible even at UV images taken with *Hubble Space Telescope* (*HST*).

(iii) *Stochastic effects*. When dealing with relatively low-populated stellar systems, it has been suggested that stochastic effects may significantly affect the comparison between models and observations. This is a wavelength-dependent effect because stars in different evolutionary phases do not affect the various spectral regions in the same way. Several papers have been devoted to the analysis of stochastic effects in evolutionary synthesis models (e.g. Chiosi, Bertelli & Bressan 1988; Cerviño et al. 2002; Cerviño & Luridiana 2004, 2006; Cerviño, Luridiana & Jamet 2008). Tuning the content of massive stars in star-forming regions via mass segregation related to stochastic effect was suggested by García-Vargas & Díaz (1994) as an alternative to an IMF steepening to decrease the number of massive stars, what helped to explain the emission line ratios observed in Giant Extragalactic high-metallicity H II regions. As we will show in Paper II, these observations can now naturally be fitted by PopStar models, without the need of introducing this effect. Moreover, observations with *HST* show evidence against these stochastic effects in star-forming regions, since very massive stars have been detected even in small clusters (e.g. Walborn, Maíz-Apellániz & Barbá 2002; Úbeda, Maíz-Apellániz & MacKenty 2007).

We have defined stellar groups along each isochrones: massive stars with initial mass larger than 20 $M_\odot$; OB stars when their effective temperature is $T_{\rm eff} \geq$ 25 000 K; red supergiants (RSG) if $T_{\rm eff} <$ 6760 K; WR stars are split into WN stars, when the surface hydrogen content by mass is $X < 0.3$, and WC stars when at the surface $X = 0$ and ^{12} C > ^{14} N by number. All stars more massive than 8 $M_\odot$ are supposed to die as core-collapsed supernovae (SNe). Intermediate- and low-mass ($M < 15\,M_\odot$) stars in the evolutionary phases beyond the AGB phase with $T_{\rm eff} >$ 50 000 K are named PN stars. All other stars are classified as *normal stars* (NS). This classification will be useful to assign a suitable spectrum to the corresponding star.

Table 2 shows, as an example, the time evolution of the number of massive stars, normalized to an initial cluster mass of 1 $M_\odot$, for a Salpeter IMF with $m_{\rm low} = 0.15$ and $m_{\rm up} = 100$ (SAL2) and for solar metallicity. For each age, given in logarithmic scale in Column 1, we have the number of massive stars in Column 2, OB stars in Column 3, WR WN-type stars in Column 4, WR WC-type stars in Column 5, RSG in Column 6, core-collapsed SN in Column 7 and PNe in Column 8. The general table for the whole grid of IMFs, ages and metallicities is given in electronic format (see http://cdsarc.u-strasburg.fr/cats/J.MNRAS.htx).

The strong dependence of the star counts in the different phases with the metallicity is shown in Fig. 1. Here, the numbers are normalized to the initial total number of stars in the isochrone from 0.15 to 100 $M_\odot$.

It can be seen that WR stars appear only for $Z \geq 0.004$. The RSG number also changes appreciably with metallicity: it is smaller for the lowest metallicities, but the age range at which they exist is shorter for higher values of Z. In contrast, OB and PN stars do not show large variations with the metallicity.

The effects of a different IMF are shown in Fig. 2, limited to the case of $Z = 0.02$. The slopes of the adopted IMF significantly affect the number of stars of different types. For example, the total number of SNe produced by a stellar population of 1 $M_\odot$ is 0.35×10^{-2} for the case FER, $0.53\ 10^{-2}$ for KRO, $0.87\ 10^{-2}$ for SAL2 and $0.12\ 10^{-1}$ for CHA.

The temperature distributions of *all* WN and WC stars generated by an SSP of 10^6 $M_\odot$ are shown in Figs 3 and 4, respectively. Note that the temperature is the core-hydrostatic temperature predicted by stellar evolution tracks, and it is not the one used to assign the atmosphere model, as discussed later. Also note that no WR stars are predicted for $Z = 0.0001$ and 0.0004 in the single stellar evolution scheme.

These histograms have been computed assuming an STB IMF in order to allow a direct comparison with Smith et al. (2002a). The main difference with respect to Smith et al. (2002a) is that our predicted number of WN stars, for solar metallicity, is smaller at all temperatures, but we reach higher temperatures than those calculated with the updated STB99. The different behaviour of the histograms is due to the different sets of stellar tracks adopted (Padova's for this work and Geneve's used by STB99).

Table 2. Number of stars of different type in each age. We list only the results for ages up to 5 Myr. We consider in this table numbers normalized to a cluster mass of 1 $M_\odot$, a Salpeter IMF with $m_{low} = 0.15\ M_\odot$, $m_{up} = 100\ M_\odot$ and $Z = 0.02$. A sample of the table is shown here; the table for the whole range of age and metallicity is available in the electronic version of the article (see the Supporting Information).

log Age (yr)	$N(M > 20\,M_\odot)$	N_{OB}	N_{WR-WN}	N_{WR-WC}	N_{RSG}	$N_{SNII/Ib/Ic}$	N_{PN}
5.00	2.311e−03	3.555e−03	0.000e+00	0.000e+00	0.000e+00	0.000e+00	0.000e+00
5.48	2.311e−03	3.555e−03	0.000e+00	0.000e+00	0.000e+00	0.000e+00	0.000e+00
5.70	2.311e−03	3.555e−03	0.000e+00	0.000e+00	0.000e+00	0.000e+00	0.000e+00
5.85	2.311e−03	3.555e−03	0.000e+00	0.000e+00	0.000e+00	0.000e+00	0.000e+00
6.00	2.311e−03	3.555e−03	0.000e+00	0.000e+00	0.000e+00	0.000e+00	0.000e+00
6.11	2.312e−03	3.555e−03	0.000e+00	0.000e+00	0.000e+00	0.000e+00	0.000e+00
6.18	2.311e−03	3.555e−03	0.000e+00	0.000e+00	0.000e+00	0.000e+00	0.000e+00
6.23	2.312e−03	3.555e−03	0.000e+00	0.000e+00	0.000e+00	0.000e+00	0.000e+00
6.30	2.311e−03	3.555e−03	0.000e+00	0.000e+00	0.000e+00	0.000e+00	0.000e+00
6.34	2.312e−03	3.555e−03	0.000e+00	0.000e+00	0.000e+00	0.000e+00	0.000e+00
6.40	2.312e−03	3.555e−03	0.000e+00	0.000e+00	0.000e+00	0.000e+00	0.000e+00
6.45	2.311e−03	3.520e−03	0.000e+00	0.000e+00	0.000e+00	0.000e+00	0.000e+00
6.48	2.312e−03	3.457e−03	9.522e−06	0.000e+00	0.000e+00	0.000e+00	0.000e+00
6.51	2.312e−03	3.341e−03	1.349e−05	6.036e−05	0.000e+00	0.000e+00	0.000e+00
6.54	2.285e−03	3.119e−03	1.678e−05	1.717e−04	0.000e+00	2.484e−05	0.000e+00
6.57	2.225e−03	2.956e−03	7.908e−06	2.263e−04	0.000e+00	6.030e−05	0.000e+00
6.60	2.098e−03	2.814e−03	1.563e−05	2.029e−04	0.000e+00	1.261e−04	0.000e+00
6.63	1.967e−03	2.692e−03	2.299e−05	1.997e−04	0.000e+00	1.323e−04	0.000e+00
6.65	1.897e−03	2.619e−03	3.361e−05	2.296e−04	0.000e+00	7.030e−05	0.000e+00
6.68	1.771e−03	2.484e−03	7.627e−05	1.897e−04	1.852e−06	1.263e−04	0.000e+00
6.70	1.670e−03	2.396e−03	1.524e−04	8.767e−05	2.212e−06	1.021e−04	0.000e+00

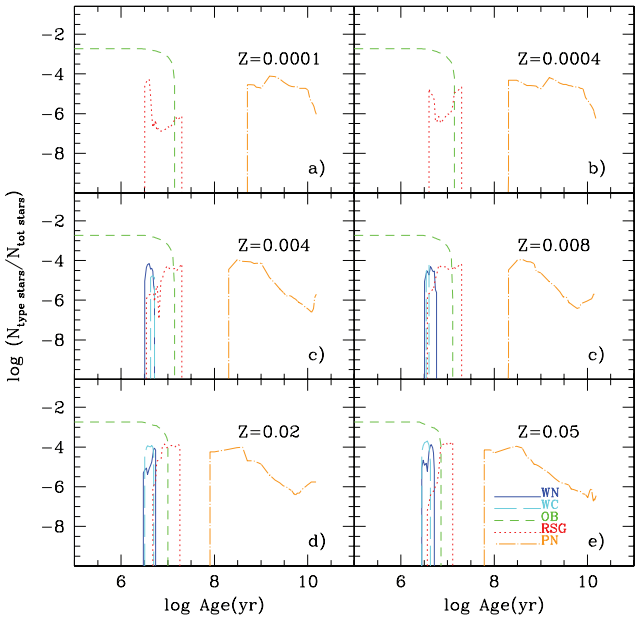

Figure 1. Logarithm of the ratio between different types of stars and the total number of stars along 15 Gyr evolution. SSPs computed for IMF by Salpeter with $m_{low} = 0.15\,M_\odot$, $m_{up} = 100\,M_\odot$ and six metallicities, Z: (a) 0.0001, (b) 0.0004, (c) 0.004, (d) 0.008, (e) 0.02 and (f) 0.05.

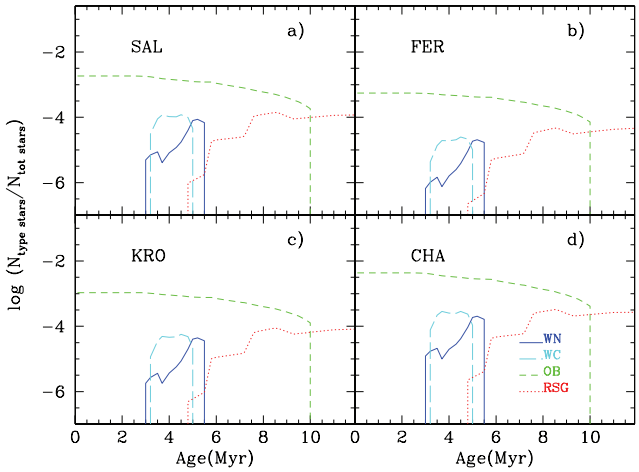

Figure 2. Logarithm of ratio between different types of stars and the total number of stars, along the first 5 Myr of the cluster evolution for solar metallicity ($Z = 0.02$) and four different IMFs: (a) SAL2, (b) FER, (c) KRO and (d) CHA. All of them defined in the same mass range, between $m_{low} = 0.15\,M_\odot$ and $m_{up} = 100\,M_\odot$.

2.2 Synthesis code description

To compute the integrated properties of SSPs, we have used the synthesis code by García-Vargas et al. (1998), updated by MGV00, together with a revised version of the atmosphere models and of the nebular emission contribution.

The main atlas of atmosphere models is from Lejeune et al. (1997), with its excellent coverage of effective temperatures, gravities and metallicities, for stars with $T_{eff} \leq 25\,000$ K. This atlas is used for all previously defined NS. For O, B and WR stars, we have taken the NLTE blanketed models by Smith et al. (2002a), for $Z = 0.001$, 0.004, 0.008, 0.02 and 0.04. There are 110 models for OB stars, with 25 000 K $T_{eff} \leq$ 51 500 K and $2.95 \leq \log g \leq 4.00$, calculated with the code by Pauldrach, Hoffmann & Lennon (2001), and 120 models for WR stars (60 WN + 60 WC), calculated with the code CMFGEN by Hillier & Miller (1998), with $30\,000 \leq T^* \leq 120\,000$ K and $1.3 \leq R^* \leq 20.3\,R_\odot$ for WN, and with $40\,000 \leq T^* \leq 140\,000$ K and $0.8 \leq R^* \leq 9.3\,R_\odot$ for WC. T^* and R^* are the temperature and the radius at a Roseland optical depth of 10.

For P-AGB and PN stars, we have used the NLTE models by Rauch (2003). In this library, the effective temperature goes from 50 000 to 190 000 K and $\log g$ is between 5.00 and 8.00. For higher

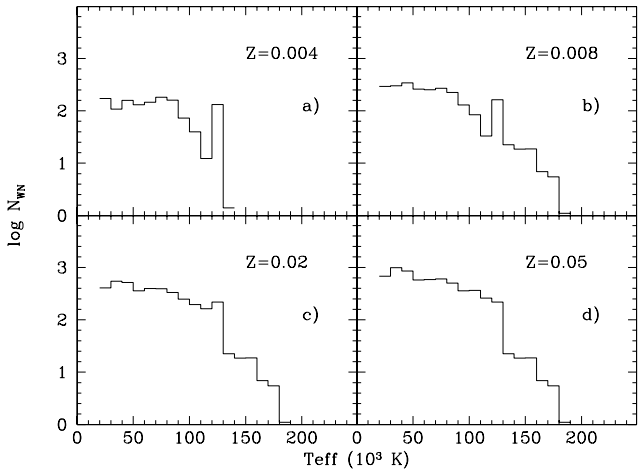

Figure 3. Total number of WR WN-type stars produced by a stellar population of 10^6 $M_\odot$ for an STB IMF, as a function of the hydrostatic temperature of the star. Different panels correspond to different metallicities, Z: (a) 0.004, (b) 0.008, (c) 0.02 and (d) 0.05.

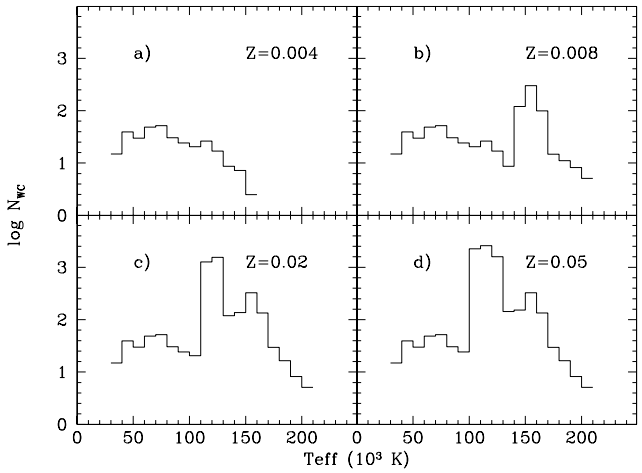

Figure 4. Total number of WR WC-type stars produced by a stellar population of 10^6 $M_\odot$ for an STB IMF, as a function of the hydrostatic temperature of the star. Different panels correspond to different metallicities, Z: (a) 0.004, (b) 0.008, (c) 0.02 and (d) 0.05.

temperatures, we use blackbodies. These models include all elements from H to Ni, and they are available for two values of metallicities: $Z = 0.002$ and 0.02. We have used the first metallicity spectra for our three metal-poor isochrones $Z = 0.0001$, 0.0004 and 0.004, and the solar abundance spectra for the three other metallicity isochrones, $Z = 0.008$, 0.02 and 0.05.

To assign the spectrum to the star along the isochrone, we proceed as follows. We select the more appropriate model in $T_{\rm eff}$ and $\log g$ in the corresponding spectral library following the definition of groups of stars. However, for NS with $T_{\rm eff} \geq 63\,000$ K and an initial mass $\geq 15\,M_\odot$ we use the WN stars models; for NS with initial mass $\leq 15\,M_\odot$ and $T_{\rm eff} \geq 50\,000$ or 31 600 K and gravity $\log g > 8$, we use the PN spectral models, and for WR stars with $T_{\rm eff} < 30\,000$ K, we assign an OB spectrum.

Fig. 5 shows, for solar abundance, the values of gravity and effective temperature of the selected stellar models for NS and for those stars which end their life as PN, as red and green dots, respectively, overplotted over the effective-temperature–gravity plane of the same kind of stars existing in the Hertzsprung–Russell (HR)

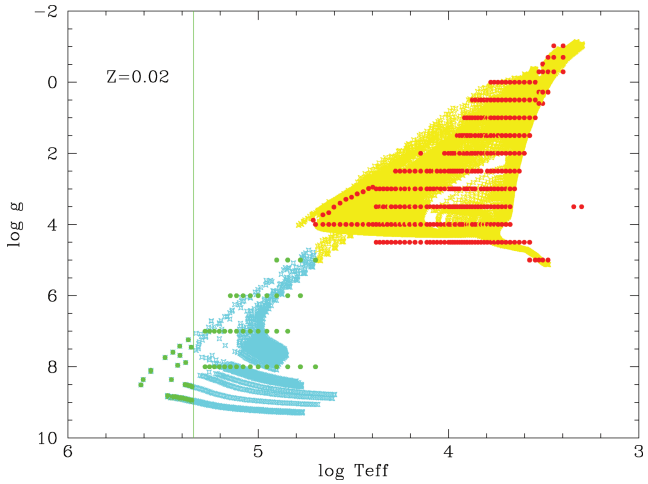

Figure 5. Model assignation for $Z = 0.02$: yellow and cyan asterisks correspond to NS, and those which end their life as PN, respectively, according to Padova isochrones. The available atmosphere models for these stars are shown overplotted as red and green solid dots. Note that the coverage is good enough. Additional panels for Fig. 5 corresponding to $Z = 0.05$, 0.008, 0.004, 0.0004 and 0.0001, respectively, are given in electronic format (see the Supporting Information).

diagrams used as inputs of our code, as yellow and cyan asterisks. The solid green line at the left-hand part of the figure delimits the upper temperature above which there is no model for PN stars. We assign a blackbody spectrum to the stars located on the left of this line. The same figures for the other metallicities are in electronic format.

When the stellar wind is optically thick, as in the case of WR stars, the isochrone effective temperature cannot be used to assign a stellar model, since isochrones give the hydrostatic $T_{\rm eff}$, while atmospheres use the effective temperature at a Rosseland optical depth of 10, R^*. In that case, to assign a model to each WR star, we use the relationships among optical depth τ, mass loss, $\mathrm{d}M/\mathrm{d}t$ and wind velocity, $v(r)$:

$$\mathrm{d}\tau = -\kappa(r)\rho(r)\,\mathrm{d}r, \tag{5}$$

where $\kappa(r) = 0.2(1 + X_{\rm S})$ and $X_{\rm S}$, the H surface abundance by mass (assumed 0.2 for WN and 0 for WC). The mass conservation requires

$$\dot{M} = \frac{\mathrm{d}M}{\mathrm{d}t} = 4\pi r^2 \rho(r) v(r)\,\mathrm{d}r. \tag{6}$$

Assuming for the wind velocity the form $v(r) = v_\infty(1 - R_{\rm S}/r)^\beta$ with $\beta = 2$ (Bressan, Chiosi & Bertelli 1984), and integrating these equations, we find the relation between R^* and the stellar radius, $R_{\rm S}$, as

$$R^* = R_{\rm S}\left[1 + \frac{0.02(1 + X_{\rm S})\dot{M}}{4\pi v_\infty R_{\rm S}}\right]. \tag{7}$$

This is the radius we use to select the atmosphere model.

The first result of the evolutionary synthesis code is an HR table for each age and metallicity, providing the basic quantities along the isochrones. As an example, Table 3, for $Z = Z_\odot$ and age of 0.1 Myr, provides for each stellar mass (Column 1), the effective temperature (Column 2), gravity (Column 3) and the luminosity (Column 4) of the isochrone, and the values of the corresponding spectral model in Columns 5–7, respectively. Column 8 gives the mass-loss rate. The star type is given in Column 9. The last six columns, 10 to 15, give the number of stars in each HR diagram

Table 3. HR diagram for stars with $50 \leq M \leq 75\,M_{\odot}$ and $Z_{\odot}$ and an age of 0.1 Myr (log Age = 5.00). The whole table is available in electronic format together with the complete set of HR diagrams.

Mass$_*$-HR ($M_{\odot}$)	$T_{\rm eff}$-HR (K)	log g-HR	log L-HR ($L_{\odot}$)	$T_{\rm eff}$-Mod (K)	log g-Mod	log L-Mod ($L_{\odot}$)	log($\dot{M}$)	WR	N_* SAL1	N_* SAL2	N_* FER	N_* KRO	N_* CHA	N_* STB
50.30	44 771.33	4.13	5.57	50 000	4.00	5.60	−5.903	NS	2.020e−05	1.010e−05	1.960e−06	4.050e−06	1.520e−05	2.190e−05
50.80	44 874.54	4.13	5.58	50 000	4.00	5.61	−5.892	NS	1.970e−05	9.840e−06	1.900e−06	3.940e−06	1.480e−05	2.140e−05
51.30	44 977.97	4.13	5.59	50 000	4.00	5.61	−5.881	NS	1.920e−05	9.620e−06	1.850e−06	3.840e−06	1.450e−05	2.090e−05
51.80	45 081.65	4.12	5.60	50 000	4.00	5.62	−5.870	NS	1.880e−05	9.400e−06	1.790e−06	3.740e−06	1.420e−05	2.050e−05
52.30	45 185.62	4.12	5.61	50 000	4.00	5.62	−5.860	NS	1.840e−05	9.190e−06	1.740e−06	3.640e−06	1.390e−05	2.000e−05
52.80	45 185.62	4.12	5.61	50 000	4.00	5.63	−5.849	NS	1.800e−05	8.990e−06	1.700e−06	3.550e−06	1.360e−05	1.960e−05
53.30	45 289.77	4.12	5.62	50 000	4.00	5.64	−5.839	NS	1.760e−05	8.790e−06	1.650e−06	3.460e−06	1.330e−05	1.910e−05
53.80	45 394.17	4.12	5.63	50 000	4.00	5.64	−5.828	NS	1.720e−05	8.600e−06	1.600e−06	3.380e−06	1.300e−05	1.870e−05
54.30	45 498.80	4.12	5.64	50 000	4.00	5.65	−5.818	NS	1.680e−05	8.410e−06	1.560e−06	3.290e−06	1.270e−05	1.830e−05
54.80	45 603.68	4.12	5.65	50 000	4.00	5.65	−5.808	NS	1.650e−05	8.230e−06	1.520e−06	3.210e−06	1.240e−05	1.790e−05
55.30	45 708.80	4.12	5.66	50 000	4.00	5.66	−5.798	NS	1.610e−05	8.060e−06	1.480e−06	3.130e−06	1.220e−05	1.760e−05
55.80	45 708.80	4.11	5.67	50 000	4.00	5.66	−5.788	NS	1.580e−05	7.890e−06	1.440e−06	3.060e−06	1.190e−05	1.720e−05
56.30	45 814.16	4.11	5.68	50 000	4.00	5.67	−5.778	NS	1.550e−05	7.730e−06	1.400e−06	2.990e−06	1.170e−05	1.680e−05
56.80	45 919.82	4.11	5.68	50 000	4.00	5.67	−5.768	NS	1.510e−05	7.570e−06	1.370e−06	2.920e−06	1.150e−05	1.650e−05
57.30	46 025.67	4.11	5.69	50 000	4.00	5.68	−5.758	NS	1.480e−05	7.420e−06	1.330e−06	2.850e−06	1.120e−05	1.620e−05
57.80	46 131.76	4.11	5.70	50 000	4.00	5.68	−5.748	NS	1.450e−05	7.260e−06	1.300e−06	2.780e−06	1.100e−05	1.580e−05
58.30	46 238.10	4.11	5.71	50 000	4.00	5.69	−5.738	NS	1.420e−05	7.120e−06	1.270e−06	2.720e−06	1.080e−05	1.550e−05
58.80	46 238.10	4.10	5.72	50 000	4.00	5.70	−5.729	NS	1.400e−05	6.980e−06	1.240e−06	2.660e−06	1.060e−05	1.520e−05
59.30	46 344.68	4.10	5.73	50 000	4.00	5.70	−5.719	NS	1.370e−05	6.840e−06	1.210e−06	2.600e−06	1.040e−05	1.490e−05
59.80	46 451.51	4.10	5.74	50 000	4.00	5.71	−5.710	NS	1.340e−05	6.710e−06	1.180e−06	2.540e−06	1.020e−05	1.460e−05
60.30	46 558.63	4.10	5.74	50 000	4.00	5.71	−5.702	NS	1.320e−05	6.580e−06	1.150e−06	2.480e−06	9.990e−06	1.430e−05
60.80	46 558.63	4.10	5.75	50 000	4.00	5.71	−5.697	NS	1.290e−05	6.450e−06	1.120e−06	2.430e−06	9.800e−06	1.400e−05
61.30	46 558.63	4.10	5.75	50 000	4.00	5.72	−5.691	NS	1.270e−05	6.330e−06	1.090e−06	2.370e−06	9.620e−06	1.380e−05
61.80	46 558.63	4.10	5.76	50 000	4.00	5.72	−5.686	NS	1.240e−05	6.210e−06	1.070e−06	2.320e−06	9.440e−06	1.350e−05
62.30	46 665.95	4.10	5.76	50 000	4.00	5.72	−5.680	NS	1.220e−05	6.090e−06	1.040e−06	2.270e−06	9.270e−06	1.330e−05
62.80	46 665.95	4.10	5.77	50 000	4.00	5.73	−5.675	NS	1.200e−05	5.980e−06	1.020e−06	2.220e−06	9.100e−06	1.300e−05

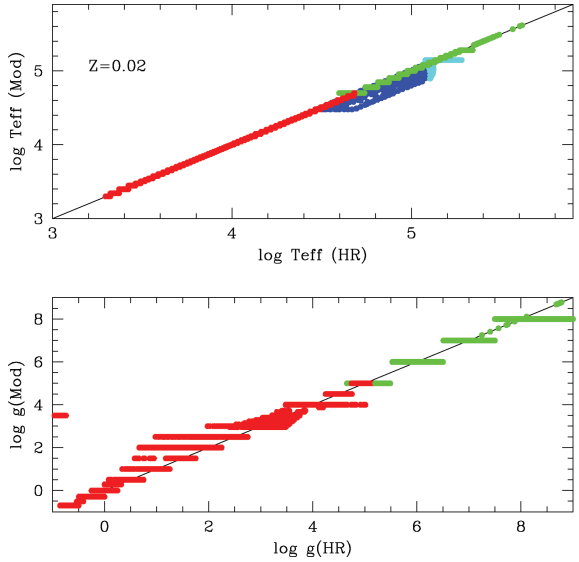

Figure 6. Upper panel: effective temperature assigned to each star as a function of the corresponding $T_{\rm eff}$ in the isochrone, for solar abundance as labelled. Bottom panel: same comparison for stellar gravity values.The other abundance figures are given in electronic format.

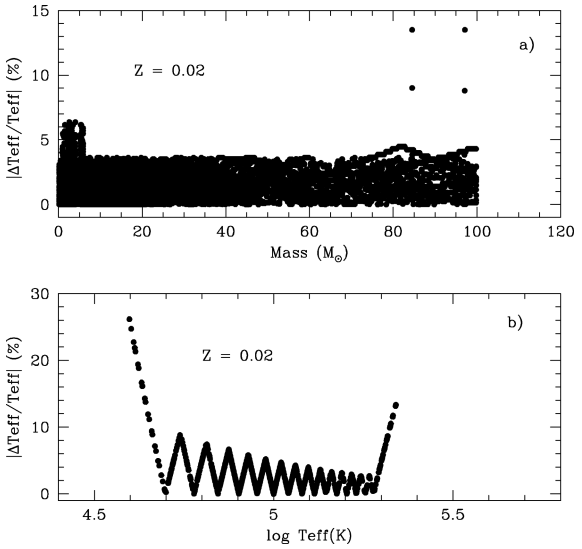

Figure 7. Assignation error, in percentage, in the effective temperature for solar abundance; (a) NS as a function of their masses and (b) P-AGB stars (PN), as a function of $T_{\rm eff}$.

point for each one of our six IMFs. The complete set of tables for all ages and metallicities is given in electronic format. In the assignation process, the luminosity of the star along the isochrone is preserved, and therefore differences between Columns 4 and 7 values are not significant.

Fig. 6 shows the comparison between the theoretical (isochrone's) versus the assigned (stellar atmosphere model's) values for solar abundance. Additional panels of Fig. 6 corresponding to $Z = 0.05$, 0.008, 0.004, 0.0004 and 0.0001 are in electronic format (see the Supporting Information). The upper panel depicts the assigned effective temperature (stellar atmosphere model) as a function of the original effective temperature (isochrone's $T_{\rm eff}$), in the HR diagram. The black solid line indicates the identity. Red dots represent NS, while green dots are PNs. In both cases, they fall over the identity line. WR stars (WC as cyan dots and WN as blue dots, respectively) fall slightly below this line, which is reasonable since the temperature given in the stellar models is the temperature at this same Rosseland opacity equal to 10, lower than the hydrostatic $T_{\rm eff}$ from the isochrone. The bottom panel shows an equivalent plot but for the gravity (without WR stars).

Fig. 7 illustrates the assignation errors in the effective temperature, for solar abundance. Additional panels of Fig. 7 for other metallicities are given in electronic format (see the Supporting Information). The error in the assigned effective temperature as a function of the initial stellar mass, given by the difference between columns (2) and (5) of the tables, is below 10 per cent for NS (Fig. 7a), and it is even smaller than 5–7 per cent in most of them except for some very metal-poor massive stars, for which it reaches a 15 per cent, and for the lowest mass stars, which are likely in the border of the PN region. In the first case, the increase in this error of temperature results from the fact that there are no atmosphere models for NS, hotter than 51 000 K. All models above this temperature correspond to WR stars, but the hottest stars for $Z = 0.0001$ and 0.0004 are not WR stars, and therefore an NS atmosphere model with a smaller temperature has been assigned to them. For the PN stars (Fig. 7b), the error, as a function of the effective temperature, is slightly larger, mostly at the temperature boundaries. The main reason is that the temperature grid for PN atmosphere models is coarser than that of NS.

2.3 Mechanical energy injection and associated H II region

From the number of massive (O, B and WR) stars and SN, we can directly compute the rate of mechanical energy injected into the interstellar medium (ISM) by stellar winds and SN explosions. At each age, τ, the energy injection rate by stellar winds is

$$\frac{{\rm d}E_W}{{\rm d}t}(\tau) = \sum_{M_*} 0.5\dot{M}(M_*)v^2_{\rm inf}(M_*) * n_{\rm WR}(M_*), \quad (8)$$

where M_*, $n_{\rm WR}(M_*)$ and $\dot{M}$ are the initial mass and number along the isochrone, and the current mass-loss rate, respectively. The energy injection rate is obtained after adding to equation (8) the energy contribution by the SN rate

$$\frac{{\rm d}E}{{\rm d}t}(\tau) = \frac{{\rm d}E_W}{{\rm d}t} + \epsilon_{\rm SN}\frac{{\rm d}n_{\rm SN}}{{\rm d}t}, \quad (9)$$

where $\epsilon_{\rm SN}$ is the energy injected by a single SN event and $\frac{{\rm d}n_{\rm SN}}{{\rm d}t} = \nu_{\rm SN}(\tau)$ is the SN rate or number of SN in each time-step, given in Table 2.

We can derive the radius of the associated HII region from the mechanical energy produced by the expanding atmospheres of massive stars with strong winds. Castor, McCray & Weaver (1975) demonstrated that an early-type star with a strong stellar wind can blow out a large cavity or bubble in the surrounding gas, if it is assumed to be compressed into a thin spherical shell. The wind-driven shell begins to evolve with an initial phase of free expansion followed by an adiabatic expansion phase, and then the material collapses into a thin, cold shell as a result of radiative cooling.

At this stage, the gas traps the ionization front and the radiative phase begins. In this phase, the ionizing photons are absorbed and the region cools via emission in the Balmer lines. In this process, the radius of the outer shock, $R_{\rm H\,II Reg}$ evolves as

$$R_{\rm H\,II Reg} = 1.6(\epsilon/n)^{1/5}\tau^{3/5}({\rm pc}), \quad (10)$$

where $\epsilon = \frac{{\rm d}E}{{\rm d}t}(\tau)$ is the total mechanical energy (SN and stellar winds) per unit time injected in units of 10^{36} erg s^{-1}, calculated

Table 4. Mechanical energy injected into the ISM by a stellar cluster of $1\,M_\odot$ due to massive star winds and to SN explosions, and the corresponding H II region radius for the first 5 Myr, an IMF SAL2 and solar metallicity. A sample of the table is shown here; the full table is available in the electronic version of the article (see the Supporting Information).

log(Age) (yr)	$E_{\mathrm{mec_{SN}}}$	$E_{\mathrm{mec_{Wind}}}$ (10^{47} erg)	$E_{\mathrm{mec_{tot}}}$	$R_{\mathrm{H\,IIreg}}$ (pc)
5.00	0.0000	0.0968	0.0968	1.26
5.48	0.0000	0.2613	0.2613	2.39
5.70	0.0000	0.4193	0.4193	3.22
5.85	0.0000	0.6800	0.6800	4.06
6.00	0.0000	1.2113	1.2113	5.26
6.11	0.0000	2.2210	2.2210	6.59
6.18	0.0000	2.4558	2.4558	7.12
6.23	0.0000	2.5839	2.5839	7.57
6.30	0.0000	3.3025	3.3025	8.48
6.34	0.0000	3.1173	3.1173	8.71
6.40	0.0000	3.8874	3.8874	9.58
6.45	0.0000	4.6465	4.6465	10.39
6.48	0.0000	4.4463	4.4463	10.59
6.51	0.0000	8.9305	8.9305	12.49
6.54	0.2484	24.3092	24.5576	15.85
6.57	0.6030	34.6753	35.2783	17.42
6.60	1.2607	38.7365	39.9972	18.43
6.63	1.3229	41.0796	42.4025	19.19
6.65	0.7030	51.0340	51.7370	20.34
6.68	1.2626	52.8720	54.1346	21.06
6.70	1.0206	33.6511	34.6717	19.58

with equation (9), n is the ISM density in units of cm^{-3} and τ is the age of the shell in units of 10^4 yr. We have extrapolated this bubble geometry to a shell structure formed by the combined effects of the mechanical energy deposition from the winds coming from massive stars in the ionizing cluster and from SN explosions. Then, the ionized gas is assumed to be located in a thin spherical shell at that distance from the ionizing source.

Table 4 gives the results of these calculations. We show for each age (Column 1) the mechanical energy corresponding to the SN explosions (Column 2), the same from stellar winds (Column 3), and total (Column 4). The radius, in pc, of the H II region produced by this energy and calculated as described above is given in Column 5. The energy scales with the mass of the stellar cluster, and therefore the radius of the H II region depends on this mass as $M^{1/5}$, which must be taken into account when using this table. We show here only the results for the first 5 Myr of the evolution of a stellar cluster of $1\,M_\odot$ with IMF SAL2 and solar metallicity. The complete set of tables for all ages, metallicities and IMFs is given in electronic format.

2.4 Stellar spectral energy distributions

We have obtained the spectral energy distributions (SEDs) of SSPs for different ages (from $\log\tau = 5.00$ to 10.18), metallicities ($Z = 0.0001, 0.004, 0.004, 0.008, 0.02, 0.05$) and for several assumptions concerning the IMF (Table 1). Fig. 8 shows spectra for selected ages for $Z = Z_\odot$ and adopting the SAL2 IMF. The new SEDs are less hard than our previous models (García-Vargas et al. 1998; MGV00) because of the use of the NLTE model atmospheres of massive stars. Above 54 ev, the emergent flux is determined by the wind density as a function of metallicity and, in the NLTE models, the hardness of ionizing radiation decreases. The models produce a lower flux in the He I continuum, for $Z > 0.4\,Z_\odot$ and age < 7 Myr. The consequence of using the new models will be a lower excitation in H II regions ionized by young clusters. Our previous models, with hotter atmospheres for massive stars (García-Vargas et al. 1995), could explain the emission line ratios observed in high-metallicity H II regions, only assuming a steepening of the IMF (i.e. a smaller number of massive stars) or invoking mass segregation effects in small clusters. Today, we know that this is against evidence since *HST* discovered very massive stars also in small clusters. The new models will explain these observations in a more natural way, as we will show in Paper II.

On the other hand, when PNe appear between $\log\tau = 8.30$ and 10.00, the SEDs are harder than in our previous models. This is due to the new models from Rauch (2003), especially computed for these very hot stellar evolution phases. Differences due to the adopted IMF are shown in Fig. 9 for three selected ages and for $Z_\odot$. They may be significant because of the different contribution

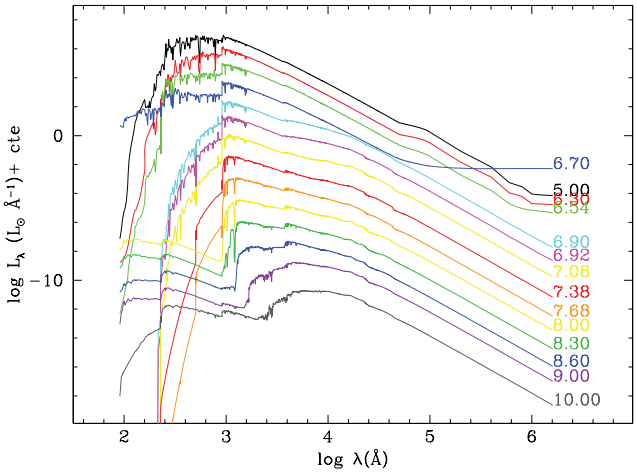

Figure 8. Stellar SEDs for the SAL2 IMF and for $Z_\odot$ at the ages labelled in the panel.

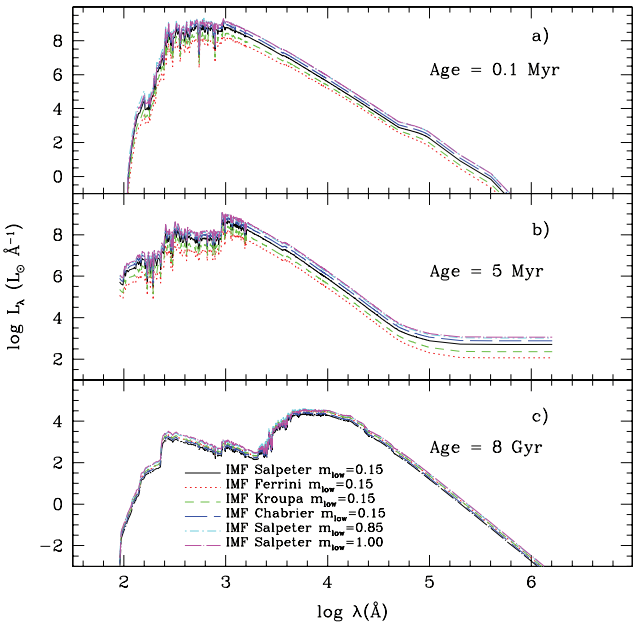

Figure 9. Comparison of the resulting SED obtained with the six IMFs for an age of (a) 0.1 Myr, (b) 5 Myr and (c) 8 Gyr.

of massive stars in the young isochrones and of low-mass stars in the old isochrones.

3 NEBULAR PLUS STELLAR SPECTRAL ENERGY DISTRIBUTIONS

In this section, we describe how we include the H and He nebular continua, free–free, free–bound and two-photon emission mechanisms, to the SED of SSPs.

3.1 Nebular contribution calculation

We first compute the total number of ionizing photons, Q(H), Q(He I), Q(He II) and Q(O I), by integrating the specific photon luminosity of a given SED from $\lambda = 0$ to 912, 504, 228 and 353.3 Å, respectively. The evolution of the numbers of ionizing photons for the six metallicities and the six IMFs is given in electronic format. Table 5 shows as an example the results for the SAL2 IMF and $Z = Z_{\odot}$ and for the first 5 Myr. For each age (Column 1), we provide the number of ionizing photons, Q(He II), Q(O I), Q(He I) and Q(H), in Columns 2 to 5, respectively. These quantities are also plotted in Fig. 10 for the first 5 Myr. These numbers are higher at low than at high metallicities, and show a smooth evolution with age. At the highest metallicities, there are abrupt variations, especially for Q(He II) and Q(O I), synchronized with the appearance of the WR phase.

Effects of different IMF are shown in Fig. 11 limited to the hydrogen ionizing photon flux. The differences mirror the different number of massive stars for a given cluster initial mass, and its different evolution with time.

Once Q(H) has been computed, we can calculate the nebular contribution. We have included the hydrogen and helium (both He and He^+) free–free and free–bound emission processes as well as the two-photon continuum. We have used the expression from Osterbrock (1989):

$$L_{\lambda}(\mathrm{erg\,s^{-1}\,\AA^{-1}\,M_{\odot}^{-1}}) = \Gamma \times \frac{c}{\lambda^2 \alpha_{\mathrm{B}}(\mathrm{H\,I})} Q(\mathrm{H}), \quad (11)$$

where Q(H) is the number of ionizing photons, c is the light velocity and α_{B} is the recombination coefficient to the excited level in hydrogen, which depends on the electronic temperature. For the latter, we have used values that depend on the metallicity, as summarized in Table 6.

The function Γ is the sum of the emission coefficients for hydrogen and helium, including both free–free and free–bound contributions, and the emission coefficient due to the two-photon continuum. That is $\Gamma = \Gamma(\mathrm{H\,I}) + \Gamma(\mathrm{He\,I}) \times \frac{N(\mathrm{He\,II})}{N(\mathrm{H})} + \Gamma(2q)$. The last function $\Gamma(2q)$ coefficient is also taken from Osterbrock (1989):

$$\Gamma(2q) = \frac{\alpha_{\mathrm{eff}} g_{\nu}}{1 + q_2/A_{2q}} \quad (12)$$

with the coefficient $A_{2q} = 8.2249$. The values of α_{eff} and q_2 also depend on the electronic temperature (Table 6). We have used the values given by Osterbrock (1989) and have performed a linear fitting, obtaining

$$\alpha_{\mathrm{eff}} = 0.647 \times 10^{-10} T_{\mathrm{e}}^{-0.722} \quad (13)$$

and

$$q_2 = 5.92 \times 10^{-4} - 6.1 \times 10^{-9} T_{\mathrm{e}}. \quad (14)$$

The function g_{ν} is taken from Nussbaumer & Schmutz (1984). The functions, Γ(H I) and Γ(He I), have two terms, due to free–free and free–bound emissions. The terms due to free–free emission are calculated with the classical expressions from Brown & Mathews (1970) and Osterbrock (1989).

The free–bound contributions have been computed using the recent work by Ercolano & Storey (2006). These last authors give the coefficients for the calculations of the continuous emission spectra of H I, He I and He II for energies from the first ionization threshold to the $n = 20$ threshold of hydrogen and for electronic temperatures in the range $100 \leq T_{\mathrm{e}} \leq 10^5$ K. Their results are given in tables where they tabulate the function

$$\Gamma^{+}_{fb}(\nu) = \Gamma_{fb}(\nu) 10^{34} T^{3/2} \mathrm{e}^{\Delta E/kT} = \Gamma_{fb}(\nu) 10^{40} t^{3/2} \mathrm{e}^{15.7887 \Delta E_{\mathrm{R}}/t} \quad (15)$$

being $t = T(K)/10^4$, ΔE is the difference between the photon energy and the energy of the nearest threshold of the lower energy and ΔE_{R} is the same energy difference expressed in Ryd units. We have computed the values of the function $\Gamma^{+}_{ff}(\nu)$ for H I, He I and He II by interpolating in wavelength, and for the electronic temperatures corresponding to the adopted metallicities given in Table 6. Fig. 12 shows the Γ^{+} function, used for the hydrogen. Green and red empty circles are the values tabulated by the above authors, while the filled blue squares are the values obtained by our interpolations. Then, we use equation (15) to compute $\Gamma_{fb}(\nu)$.

From these coefficients and those for the free–free emission, we have obtained the total Γ_{ff+fb} (H I+He I+He II). This total function is slightly different than the one we used in MGV00 taken from Aller (1991). Fig. 13 compares the new results (black dots) with the old results (red stars), for $T = 10\,000$ K. The total function Γ is then found when we add the two-photon contribution. This total function is shown in Fig. 14. Panel (a) displays the three nebular contributions, free–free, free–bound and two-photon, plotted as filled blue dots, red open squares and green stars, respectively for $Z = Z_{\odot}$. This function depends on the electronic temperature, and therefore changes with metallicity. Panel (b) displays the function for the six

Table 5. The number of ionizing photons Q(He II), Q(O I), Q(He I) and Q(H) emitted by a $1\,M_{\odot}$ stellar cluster with an IMF SAL2, and solar metallicity during the first 5 Myr. A sample of the table is shown here; the full table is available in the electronic version of the article (see the Supporting Information).

log Age (yr)	log Q(He II) (s^{-1})	log Q(O I) (s^{-1})	log Q(He I) (s^{-1})	log Q(H) (s^{-1})
5.00	42.26	45.12	45.76	46.46
5.48	41.94	45.03	45.74	46.45
5.70	41.92	45.02	45.74	46.46
5.85	41.89	45.00	45.74	46.46
6.00	41.46	44.64	45.70	46.44
6.10	41.32	44.59	45.65	46.44
6.18	41.11	44.48	45.56	46.40
6.24	40.85	44.37	45.46	46.37
6.30	40.70	44.25	45.37	46.33
6.35	40.23	43.98	45.18	46.26
6.40	39.81	43.80	45.07	46.21
6.44	39.94	43.75	45.01	46.19
6.48	40.77	44.12	45.07	46.18
6.51	40.30	44.55	45.23	46.12
6.54	39.09	44.80	45.34	46.03
6.57	37.61	44.73	45.28	45.94
6.60	42.84	44.70	45.19	45.80
6.63	43.24	44.71	45.18	45.72
6.65	43.40	44.74	45.21	45.70
6.68	42.94	44.73	45.17	45.64
6.70	43.26	44.74	45.12	45.65

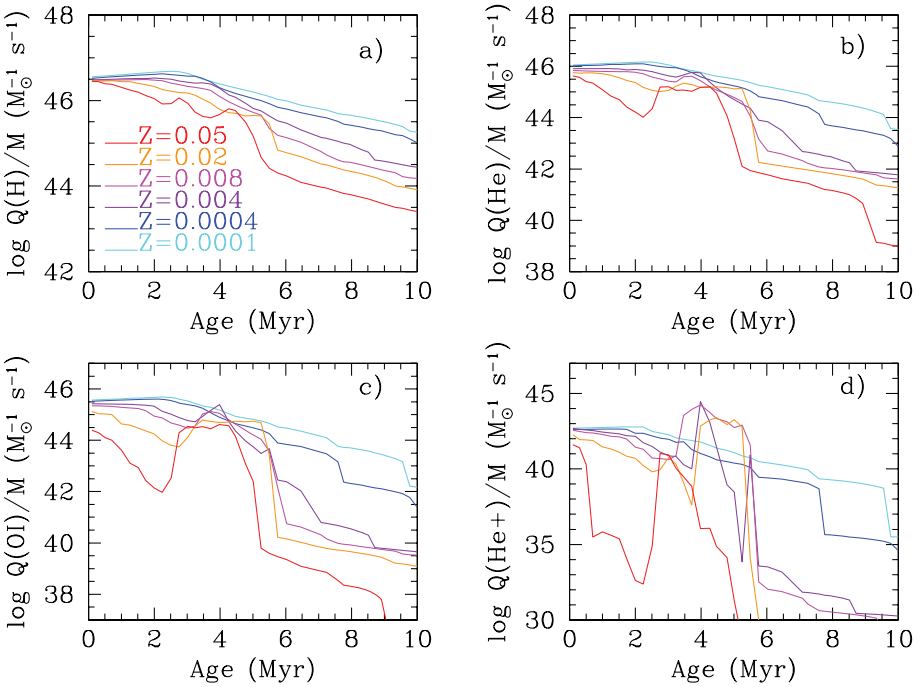

Figure 10. Time evolution of the number of ionizing photons per cluster solar mass, for SAL2 and six metallicities, for the first 5 Myr evolution. Different panels show different ionization photon evolution, labelled as (a) Q(H), (b) Q(He), (c) Q(O I) *and (d)* $Q(He^+)$.

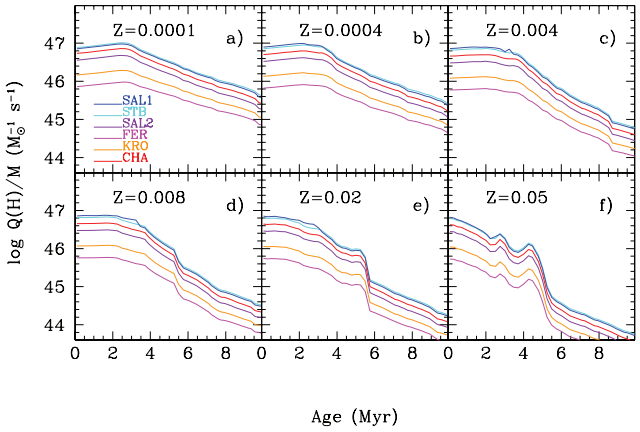

Figure 11. Time evolution for the first 5 Myr of the number of ionizing photons Q(H) for the six IMFs used in this work: (a) $Z = 0.0001$, (b) $Z = 0.0004$, (c) $Z = 0.004$, (d) $Z = 0.008$, (e) $Z = 0.02$ and (f) $Z = 0.05$.

metallicities used in this work. The metallicity affects this function only below $\lambda \sim 2000$ Å.

3.2 Luminosity and equivalent widths for H_α and H_β

We have computed the intensity of the Balmer emission lines, in particular I_{H_α} and I_{H_β}, with the following equations from Osterbrock (1989):

$$L_\beta = Q(\mathrm{H}) j_\mathrm{B}/\alpha_\mathrm{B} \tag{16}$$

and

$$L_\alpha = Q(\mathrm{H}) \frac{\alpha}{\beta} \frac{j_\mathrm{B}}{\alpha_\mathrm{B}}, \tag{17}$$

with j_β, α_B and the Balmer ratio α/β depending on the electronic temperature and, therefore, different for each metallicity. We use

Table 6. Electronic temperature assigned to each metallicity Z.

Z	T_e (K)
0.0001	19 950
0 0004	15 850
0.004	10 000
0.008	7940
0.02	6310
0.05	3160

equations (6) and (8) from Ferland (1980) for j_β and α_B. The ratio j_α/j_β is given by Osterbrock (1989).

We have measured the continuum of the stellar SEDs, S_λ, at the corresponding wavelengths, as well as the absorption line luminosity which we have subtracted from the emission line, to obtain the equivalent widths for the two lines:

$$\mathrm{EW(Å)} = \frac{(I_\mathrm{emi} - I_\mathrm{abs})(\mathrm{L}_\odot)}{S_\mathrm{cont}(\mathrm{L}_\odot \mathrm{Å}^{-1})}. \tag{18}$$

Table 7 gives the results of these calculations for a cluster mass of 1 $\mathrm{M}_\odot$, an SAL2 IMF, solar metallicity and for the first 5 Myr. The complete table is given in electronic format. This table shows for each age (Column 1), the luminosity of the H_β line in emission (Column 2) and in absorption (Column 3); the value of the continuum luminosity (stellar plus nebular) at 4860 Å (Column 4), the equivalent widths of H_β in emission (Column 5), in absorption (Column 6) and total (Column 7). Columns 8 to 13 give the same information for H_α.These results are obtained by using low-resolution spectra. That means that the equivalent width in absorption is not very precise and the errors are of the order of 5 to 10 per cent. The photoionization codes, like CLOUDY (Ferland et al. 1998), compute more precise values of emission lines and luminosities.

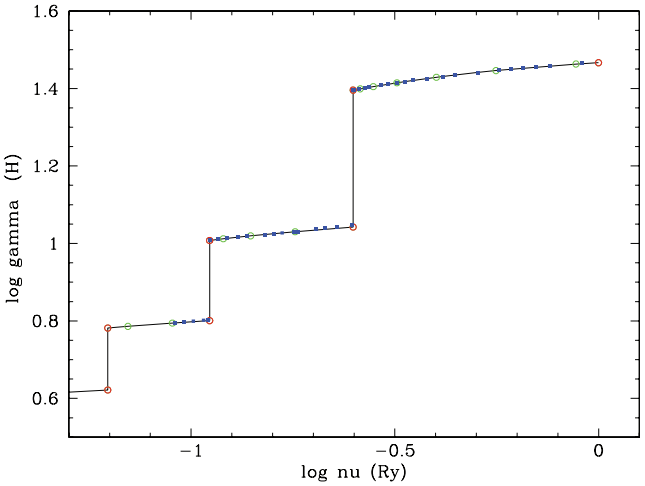

Figure 12. Γ^{+} function versus the function of the frequency ν (in Ryd), for the hydrogen free–bound nebular emission given by Ercolano & Storey (2006) as green and red open dots, and the points obtained with our interpolation to the Aller (1991) wavelengths, blue full squares, and to those used in our SEDs, solid line.

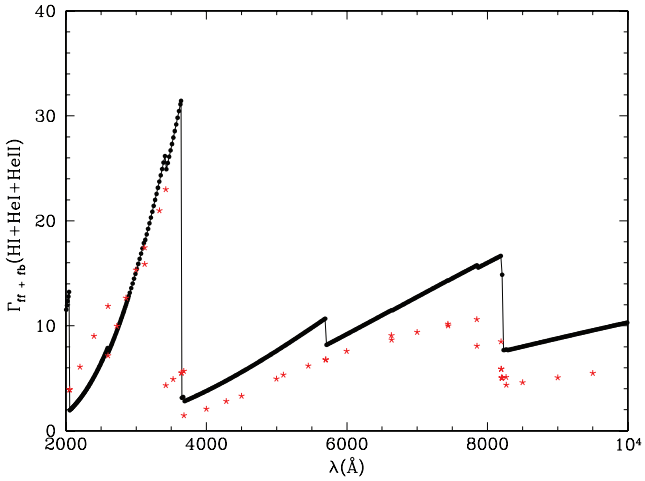

Figure 13. Free–free and free–bound nebular emission γ function for H and He obtained with the updated calculations for an electronic temperature of 10 000 K (solid black dots), compared with the old values, plotted as red stars.

3.3 Total spectral energy distributions

By adding the nebular contribution to the SSP SEDs, we have obtained the total SEDs. They are available in electronic format in http://www.fractal-es.com/SEDmod.htm and in the Virtual Observatory (VO) http://esavo.esa.int/vospec/ in compatible VO-table format as PopStar models.

Fig. 15 shows the total SEDs (arbitrary shifted for sake of clarity) for the SAL2 IMF and $Z = Z_{\odot}$ and for some selected ages. The nebular contribution is evident at the youngest ages ($\log\tau \leq 6.90$) and the ionization spectrum due to PN is also evident for the intermediate- and old-age ones ($\log\tau \geq 8.60$). Note that the spectrum of the SSP at $\log\tau = 6.70$ is dominated by WR stars.

The dependence of the total SEDs on the metallicity is shown in Fig. 16 for two selected ages. The largest differences are found at ages younger than 10 Myr, where the different contribution of the massive stars, due to different metallicities, appears. For example, at

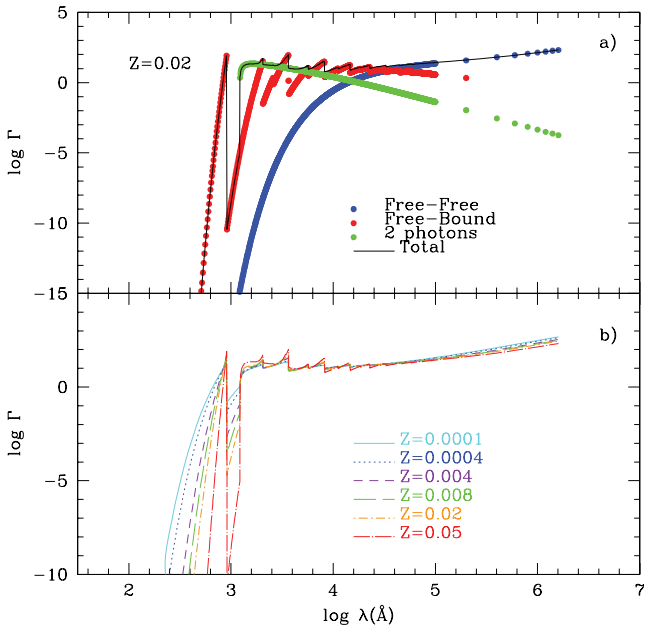

Figure 14. The total Γ function solid line, as the sum of the three contributions of nebular continuum. Panel (a) displays the three contributions: (1) free–free emission due to H and He, blue dots, (2) free–bound emission, red squares, and (3) two-photon contribution, green stars, for $Z = 0.02$. Panel (b) displays the total function for the six metallicities computed in this work as labelled in the plot.

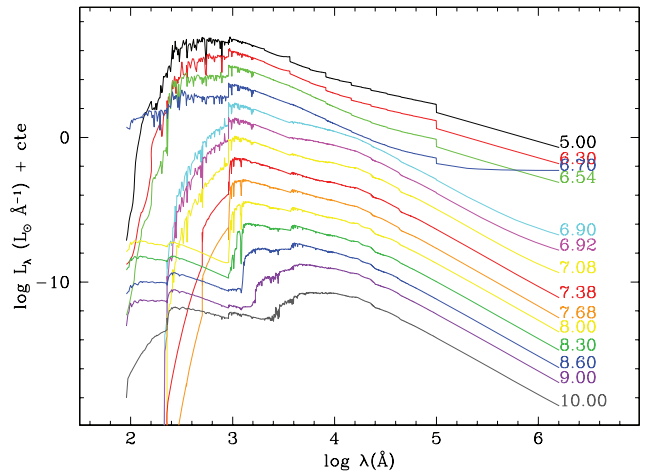

Figure 15. SEDs for SAL2 and $Z = Z_{\odot}$ including both stellar and nebular contributions at the ages labelled in logarithmic scale in the panel. Each age, starting at 0.1 Myr ($\log\tau = 5.00$), is shifted downwards by one order of magnitude, for the sake of clarity.

10 Myr low-metallicity SSPs are still capable of producing a significant nebular continuum emission. On the other hand, at these metallicities, there will not be WR single stars and, consequently, the corresponding SSP will lack their hardening effects at 5 Myr as shown in panel (a) of Fig. 16. At intermediate and old ages – panel (b) of the same figure – the differences at varying metallicity mirror the effects of composition on the temperature of the turn-off and of the RGB phase. In this respect, it is interesting to compare with the age effects to appreciate the importance of the age–metallicity degeneracy: we can see that similar variations in the SED shape are found by changing either the age (Fig. 8) or the metallicity (Fig. 15b).

Table 7. H_β and H_α emission and absorption line luminosity, continuum luminosity and equivalent widths, in emission, in absorption and total. Results are shown for the first 5 Myr evolution of a cluster whose mass has been normalized to 1 $M_\odot$ with SAL2 and $Z_\odot$. A sample of the table is shown here; the full table is available in the electronic version of the article (see the Supporting Information).

log Age (yr)	$L\mathrm{H}\beta_{\mathrm{emi}}$ ($L_\odot$)	$L\mathrm{H}\beta_{\mathrm{abs}}$ ($L_\odot$)	$S_{\mathrm{cont,H}\beta}$ ($L_\odot$ Å^{-1})	EW Hβ_{emi} (Å)	EW Hβ_{abs} (Å)	EW Hβ_{tot} (Å)	$L\mathrm{H}\alpha_{\mathrm{emi}}$ ($L_\odot$)	$L\mathrm{H}\alpha_{\mathrm{abs}}$ ($L_\odot$)	$S_{\mathrm{cont,H}\alpha}$ ($L_\odot$ Å^{-1})	EW Hα_{emi} (Å)	EW Hα_{abs} (Å)	EW Hα_{tot} (Å)
5.00	3.85	0.02	0.0080	479.26	2.66	476.60	11.49	0.25	0.0038	3002.76	64.78	2937.98
5.48	3.76	0.02	0.0082	459.45	2.54	456.91	11.22	0.24	0.0038	2914.03	61.70	2852.33
5.70	3.78	0.02	0.0083	454.63	2.53	452.10	11.29	0.24	0.0039	2893.54	61.70	2831.84
5.85	3.83	0.02	0.0085	452.14	2.52	449.63	11.42	0.24	0.0040	2883.57	61.69	2821.88
6.00	3.68	0.02	0.0088	417.89	2.54	415.35	10.97	0.25	0.0040	2730.14	61.75	2668.39
6.10	3.64	0.02	0.0091	399.45	2.53	396.92	10.85	0.25	0.0041	2643.12	61.78	2581.34
6.18	3.33	0.02	0.0094	354.16	2.57	351.59	9.94	0.25	0.0041	2415.59	61.87	2353.71
6.24	3.08	0.03	0.0098	314.93	2.59	312.34	9.20	0.26	0.0042	2208.67	61.96	2146.71
6.30	2.84	0.03	0.0105	271.55	2.60	268.95	8.46	0.27	0.0043	1961.56	62.04	1899.51
6.35	2.38	0.03	0.0110	215.76	2.63	213.13	7.11	0.27	0.0044	1619.65	62.18	1557.47
6.40	2.16	0.03	0.0120	181.14	2.62	178.52	6.46	0.29	0.0046	1394.58	62.24	1332.34
6.44	2.03	0.03	0.0131	155.79	2.65	153.13	6.07	0.31	0.0050	1221.75	62.34	1159.41
6.48	1.99	0.04	0.0140	142.07	2.63	139.45	5.92	0.33	0.0053	1124.17	61.96	1062.20
6.51	1.75	0.04	0.0143	122.29	2.74	119.55	5.21	0.33	0.0053	977.94	61.99	915.95
6.54	1.42	0.05	0.0143	99.56	3.19	96.37	4.24	0.33	0.0053	795.33	62.62	732.71
6.57	1.15	0.05	0.0139	82.70	3.53	79.17	3.43	0.33	0.0052	660.87	63.21	597.66
6.60	0.83	0.05	0.0141	58.61	3.84	54.77	2.47	0.33	0.0053	469.95	63.66	406.29
6.63	0.69	0.06	0.0135	50.75	4.15	46.60	2.05	0.32	0.0051	403.32	63.93	339.38
6.65	0.67	0.05	0.0118	56.17	4.17	52.00	1.98	0.29	0.0045	444.12	63.86	380.25
6.68	0.57	0.04	0.0098	57.98	3.84	54.14	1.70	0.23	0.0037	461.75	63.31	398.44
6.70	0.60	0.03	0.0093	63.87	3.53	60.34	1.78	0.22	0.0035	506.36	62.39	443.97

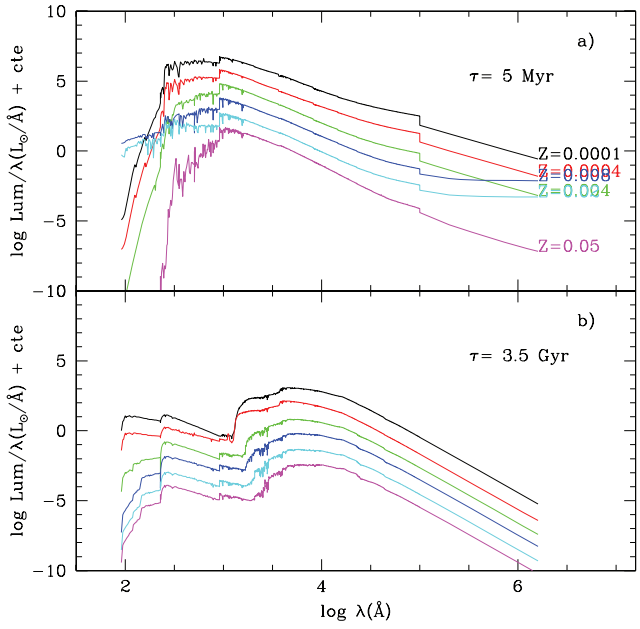

Figure 16. SEDs including both stellar and nebular contributions for an SAL2 IMF and different metallicities, as labelled. Panel (a) for 5 Myr, and panel (b) for 3.5 Gyr. Each SED is shifted downwards by 1 dex for the sake of clarity.

4 PHOTOMETRIC EVOLUTION OF STELLAR POPULATIONS

4.1 Magnitudes and colours

In this section, we provide magnitudes and colours computed for the Johnson–Cousins–Glass and for the Sloan Digital Sky Survey (SDSS) systems.

Johnson–Cousins–Glass magnitudes, *UV1*, *UV2*, *U*, *B*, *V*, *R*, *I*, *J*, *H*, *K* and *L*, are computed using the definition suitable for photon-counting devices (Girardi et al. 2002):

$$m_{R_\lambda} = -2.5 \log \frac{\int_{\lambda_1}^{\lambda_2} \lambda f_\lambda R_\lambda \mathrm{d}\lambda}{\int_{\lambda_1}^{\lambda_2} \lambda f_\lambda^0 R_\lambda \mathrm{d}\lambda} + m_{R_\lambda}^0, \quad (19)$$

where R_λ, the response function of the system, f_λ^0, the reference spectrum (Vega in this system) and its corresponding magnitudes, $m_{R_\lambda}^0$, completely define the photometric system. For the reference spectrum, we used a model atmosphere corresponding to the Vega parameters, $T_{\mathrm{eff}} = 9550$, gravity $\log g = 4$ and $Z = 0.006$, interpolated on the Lejeune et al. (1997) spectral library. Finally, absolute magnitudes were computed assuming for Vega an absolute visual magnitude of $V = 0.58$ and all colours equal to zero.

Table 8 is as an example of the absolute magnitudes for an SSP normalized to 1 $M_\odot$ $Z = 0.02$ and an SAL2 IMF. Age is in Column 1, Columns 2 and 3 refer to the two UV *HST* magnitudes *UV1* and *UV2*, and the other columns provide the *U*, *B*, *V*, *R*, *J*, *H*, *K* and *L* magnitudes. [1]

The evolution of *U*, *B*, *V* and *K* absolute magnitudes is shown in Fig. 17 for the case of the SAL2 IMF and for the six metallicities considered here. Differences among metallicities are more evident at old ages ($\tau > 1$ Gyr) except for *K* magnitude, which shows a clear dependence on *Z* also for $\tau < 1$ Gyr, due to the important contribution of RSG first and AGB, P-AGB and red giant at older ages. At very young ages, $\tau \leq 6$ Myr, an important difference is due to the contribution of nebular emission.

The evolution of the corresponding $U - B$, $B - V$, $V - R$ and $V - K$ colours is shown in Fig. 18. Besides the well-known effect

[1] Magnitude *B* is given twice, the first one is used to compute $U - B$, while the second one is used for $B - V$.

Table 8. Example of the evolution of the magnitudes in the Johnson–Cousins–Glass photometric system, for a cluster mass normalized to 1 $M_\odot$, a Salpeter IMF with $m_{low} = 0.15\ M_\odot$, $m_{up} = 100\ M_\odot$ and $Z = 0.02$. A sample of the table is shown here; the full table is available in the electronic version of the article (see the Supporting Information).

log Age (yr)	M_{UV1}	M_{UV}	M_U	M_B	M_B	M_V	M_R	M_I	M_J	M_H	M_K	M_L
5.00	−4.267	−1.973	−0.680	0.723	0.714	0.737	0.572	0.562	0.382	0.073	−0.483	−1.448
5.48	−4.311	−2.005	−0.692	0.698	0.689	0.722	0.567	0.561	0.391	0.088	−0.464	−1.424
5.70	−4.333	−2.026	−0.709	0.679	0.670	0.706	0.553	0.549	0.381	0.079	−0.471	−1.431
5.85	−4.354	−2.047	−0.727	0.660	0.650	0.688	0.537	0.533	0.366	0.065	−0.485	−1.444
6.00	−4.419	−2.106	−0.755	0.608	0.599	0.657	0.523	0.529	0.377	0.086	−0.454	−1.406
6.10	−4.463	−2.150	−0.784	0.567	0.557	0.626	0.502	0.513	0.371	0.085	−0.449	−1.397
6.18	−4.520	−2.203	−0.799	0.521	0.510	0.604	0.504	0.528	0.412	0.142	−0.375	−1.310
6.24	−4.567	−2.256	−0.824	0.469	0.458	0.573	0.495	0.531	0.441	0.187	−0.314	−1.235
6.30	−4.627	−2.327	−0.870	0.390	0.378	0.514	0.461	0.513	0.456	0.223	−0.256	−1.157
6.35	−4.691	−2.392	−0.898	0.320	0.307	0.470	0.450	0.523	0.516	0.317	−0.123	−0.991
6.40	−4.737	−2.463	−0.959	0.228	0.215	0.394	0.396	0.482	0.510	0.336	−0.072	−0.909
6.44	−4.775	−2.532	−1.033	0.128	0.116	0.305	0.323	0.419	0.474	0.322	−0.056	−0.864
6.48	−4.799	−2.578	−1.091	0.053	0.041	0.234	0.260	0.362	0.430	0.291	−0.069	−0.857
6.51	−4.743	−2.552	−1.085	0.026	0.014	0.212	0.249	0.359	0.448	0.330	−0.001	−0.750
6.54	−4.567	−2.419	−1.019	0.034	0.022	0.207	0.248	0.361	0.468	0.378	0.095	−0.592
6.57	−4.421	−2.295	−0.938	0.072	0.061	0.235	0.280	0.392	0.509	0.439	0.197	−0.429
6.60	−4.284	−2.186	−0.884	0.061	0.050	0.221	0.272	0.379	0.516	0.478	0.302	−0.217
6.63	−4.137	−2.047	−0.782	0.111	0.101	0.263	0.308	0.403	0.533	0.501	0.352	−0.112
6.65	−4.045	−1.934	−0.645	0.257	0.247	0.405	0.445	0.534	0.648	0.603	0.436	−0.061
6.68	−3.953	−1.831	−0.494	0.452	0.441	0.611	0.655	0.750	0.866	0.812	0.636	0.119
6.70	−3.925	−1.808	−0.457	0.509	0.498	0.672	0.709	0.799	0.901	0.831	0.638	0.096

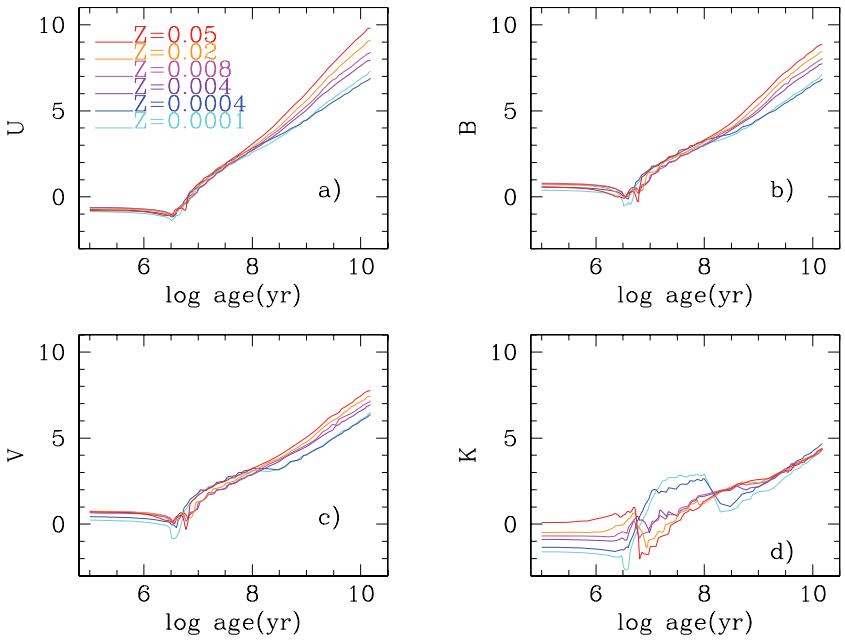

Figure 17. Magnitude evolution of magnitudes (Johnson system) for a stellar population of 1 $M_\odot$ and SAL2 IMF: (a) U, (b) B, (c) V and (d) K. In each panel, the six metallicities are shown in different colours, as labelled in panel (a).

of age–metallicity degeneracy, other two important points appear from this figure. Some colours do not increase monotonically with age. This is particularly evident for the $V - K$ colour and for solar and twice solar metallicity. The second point is the reddening of the colours (but for the $U - B$) at ages less than a few Myr. This effect, which is more pronounced at low metallicity, is due to nebular continuum emission being *relatively* more important at longer wavelengths. For example, the $V - K$ colours, without nebular emission included, saturate at $V - K \sim -0.75$ at ages below 3 Myr, for all metallicities. Thus, the inclusion of nebular emission reddens the colours of very young populations significantly. Though other effects may be at work at these young ages, like dust attenuation, it is worth stressing that, in presence of nebular emission, the colours of a very young metal-poor population are as red as those of an intermediate-age metal-rich population. These properties will be discussed in more details in the forthcoming Paper III, where photometry including the emission lines, contribution, computed in Paper II, will be calculated.

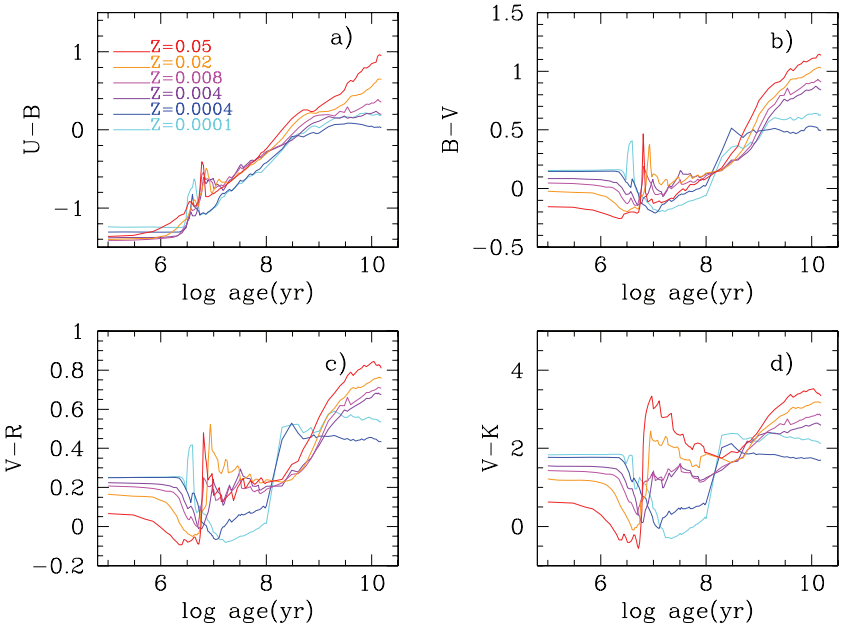

Figure 18. Colour evolution (Johnson system): (a) $U - B$, (b) $B - V$, (c) $V - R$ and (d) $V - K$. In each panel, the six metallicities are shown in different colours, as labelled in panel (a).

Absolute magnitudes in the SDSS photometric system have been calculated following Girardi et al. (2004) and Smith et al. (2002b):

$$m_{AB} = -2.5 \log \frac{\int \lambda f_\lambda R_\lambda \, \mathrm{d}\lambda}{\int \nu R_\lambda \, \mathrm{d}\lambda} - 48.60, \qquad (20)$$

where R_λ are the response curves of the SDSS filters.

An example of absolute u, g, r, I and z magnitudes, in the first 5 Myr, is provided in Table 9. Their complete evolution is shown in Fig. 19.

Magnitudes in these two photometric systems for all IMFs, ages and metallicities calculated are available in electronic format in http://www.fractal-es.com/SEDmod.htm and in compatible VO-tables.

Before concluding this section, we show, in Fig. 20, the comparison of our models against the observed integrated $V - K$ colours of LMC clusters from Persson et al. (1983), Kyeong et al. (2003), Goudfrooij et al. (2006) and Pessev et al. (2006). Cluster ages have been estimated by adopting the S-parameter calibration by Girardi et al. (1996). The black solid line is an average within suitable age bins. Models of all the metallicities considered here have been plotted. Taking into account that the oldest LMC clusters have very low metallicity, the intermediate-age clusters have $Z \sim 0.008$ and the young clusters have about solar metallicity, we may conclude that our models reproduce the observed colour evolution of LMC clusters fairly well.

In the following, we will compare our models, hereafter PopStar, with those obtained by other authors and widely used in the literature. Our comparison is limited to the models by STB99, BC03, MAR05, GON05 and with our old models by MGV00.

4.2 Comparison of results with STARBURST99

We begin our comparison with the models computed by STARBURST99 code recalling that, in its last version, STARBURST99 includes the Smith et al. (2002a) atmosphere models for massive stars, as our models. However, for the young ages, STARBURST99 makes use of the Geneva isochrones. Fig. 21 shows the first 10 Myr evolution of number of ionizing photons for H, He and He+ (top, medium and bottom panels, respectively). In each panel, our model is depicted with solid lines, while for STB99 we use long dashed lines. The blue colour lines correspond to a low-metallicity ($Z = 0.004$) case, while the red ones are for the solar metallicity ($Z = 0.02$). Differences between STB99 and this work are not very large for Q(H) and Q(He). They are more important for Q(He+) in the case of solar metallicity where our models show a more extended WR phase.

Table 9. SDSS magnitudes for the first 5 Myr of a cluster of 1 $M_\odot$, with a SAL2 IMF and $Z = 0.02$. The whole table is available in electronic format.

log τ yr	u	g	r	I	z
5.00	1.884	2.615	2.779	2.765	3.287
5.48	1.875	2.595	2.770	2.767	3.282
5.70	1.859	2.577	2.755	2.755	3.269
5.85	1.841	2.558	2.738	2.739	3.253
6.00	1.818	2.515	2.715	2.738	3.240
6.10	1.791	2.478	2.689	2.723	3.220
6.18	1.783	2.441	2.679	2.743	3.223
6.24	1.765	2.397	2.658	2.750	3.215
6.30	1.727	2.326	2.611	2.737	3.183
6.35	1.709	2.266	2.582	2.755	3.173
6.40	1.655	2.179	2.516	2.720	3.118
6.44	1.588	2.083	2.434	2.662	3.044
6.48	1.533	2.009	2.366	2.607	2.980
6.51	1.545	1.982	2.346	2.609	2.967
6.54	1.621	1.983	2.337	2.622	2.954
6.57	1.710	2.017	2.363	2.662	2.972
6.60	1.780	2.003	2.351	2.663	2.941
6.63	1.896	2.050	2.388	2.698	2.953
6.65	2.030	2.195	2.526	2.830	3.084
6.68	2.172	2.395	2.737	3.040	3.307
6.70	2.203	2.452	2.798	3.086	3.359

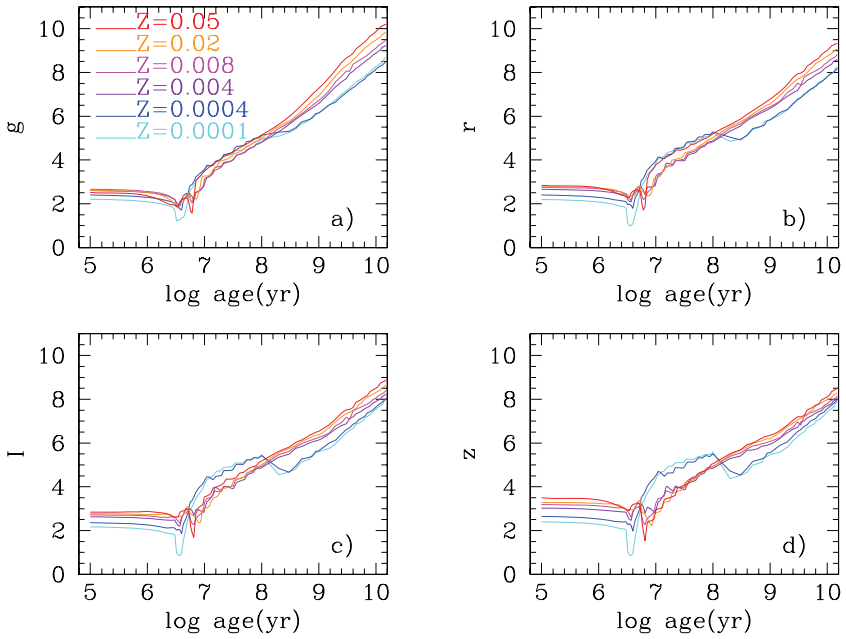

Figure 19. Evolution of SDSS magnitudes with age, for a stellar population with mass normalized to 1 $M_\odot$: (a) *g*, (b) *r*, (c) *I* and (d) *z*. In each panel, the six metallicities are shown in different colours, as labelled in panel (a).

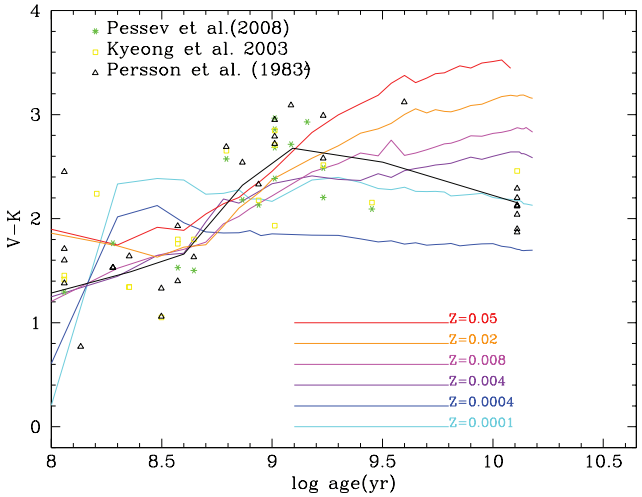

Figure 20. $V - K$ colours of SSP compared with the observed extinction-corrected colours of LMC clusters. Observed data are from authors as labelled. In some cases, the same cluster has observations from different authors.

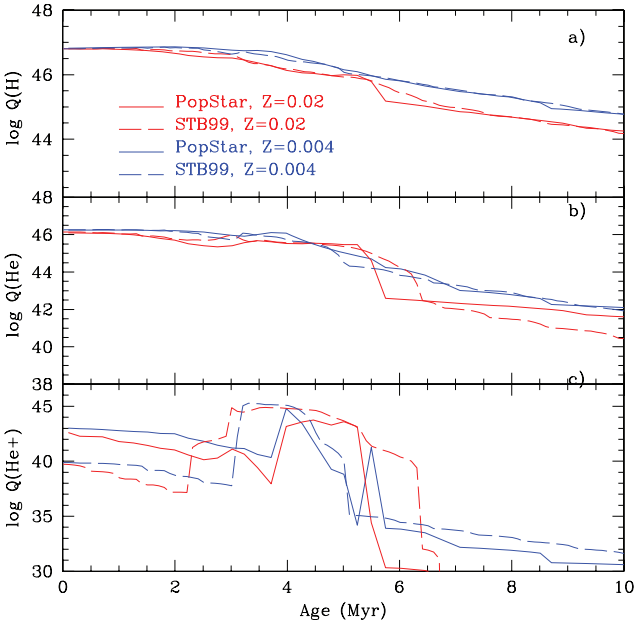

Figure 21. Comparison of the age evolution of the number of ionizing photons: (a) Q(H) (b) Q(He) and (c) Q(He+) of our models with the STB99 ones. In each panel, results for two metallicities are represented with a different line code as labelled in panel (a).

In Fig. 22, we compare our SEDs with those obtained with STB99, for some ages between 1 and 900 Myr. Panel (a) shows the case $Z = 0.004$, while panel (b) refers to $Z = 0.02$. In both cases, an STB IMF has been assumed and a normalization to a total initial mass of 1 $M_\odot$. Some differences appear at young ages, mainly due to isochrone differences as mentioned above. Remarkable differences appear at ages between 100 and 900 Myr when, in our isochrones, PNe appear. The nature of this discrepancy is certainly the higher fuel of our P-AGB stars, due to the different mass-loss rate prescriptions adopted in our revised isochrones, besides the use of the model spectra from Rauch (2003).

Fig. 23 shows the evolution of *B*, *V* and *K* magnitudes in the top, medium and bottom panels, respectively. In the left-hand panels, we show the results for $Z = 0.004$, while those for $Z = 0.02$ are shown in the right-hand panels. Our PopStar results are represented by red solid lines, while for STB99 we use blue dashed lines. Note that STB99 models are calculated only until 1 Gyr. Magnitudes *B* and *V* are practically identical in both cases. However, the *K* band shows slight differences with brighter (redder) stellar population for the youngest ages in our models compared with the STB99 ones, mostly for $Z = 0.004$, at low metallicity. The same occurs for ages $\tau > 100$ Myr: STB99 models are less bright than ours in *K* band.

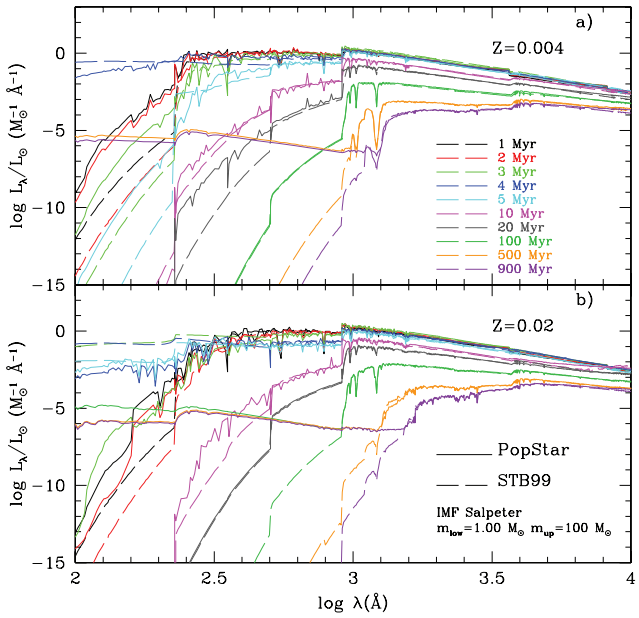

Figure 22. Comparison between SEDs obtained with PopStar and the corresponding ones from STB99 for different ages. Each age is plotted with a colour. Solid lines are PopStar models, while dashed lines are STB99 ones.

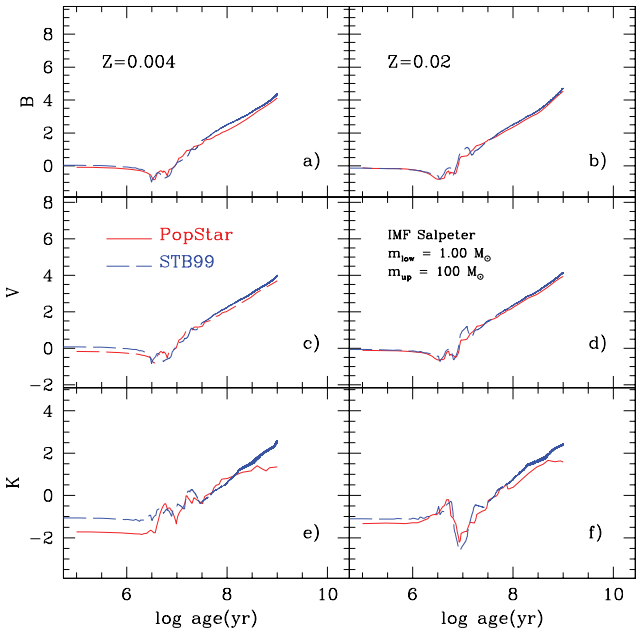

Figure 23. Magnitude evolution in *B*, *V* and *K* bands obtained in this work compared with the corresponding from STB99. Solid red lines are PopStar models, while the dashed blue lines are STB99 ones.

The comparison of the $U-B$, $B-V$, $V-R$, $V-I$ and $V-K$ colours is shown in Fig. 24, adopting the same notation for the models. The agreement is good. However, at solar metallicity there are some differences in the RSG colours (especially $V-K$) while, at low metallicity, there are differences in the AGB phase (likely caused by different mass-loss rates) and at very young ages (likely caused by differences in nebular emission continuum contribution).

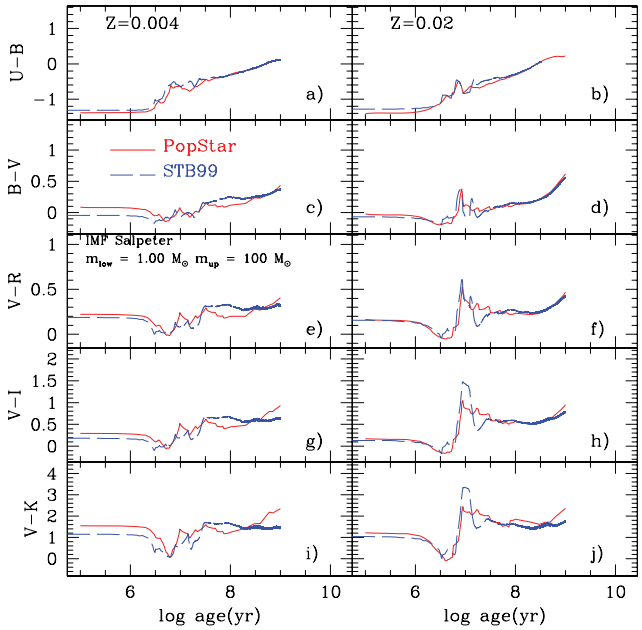

Figure 24. Colour evolution $U-B$, $B-V$, $V-R$, $V-I$ and $V-K$ obtained in this work compared with the ones in STB99. Solid red lines are PopStar results, while the dashed blue lines are STB99 ones.

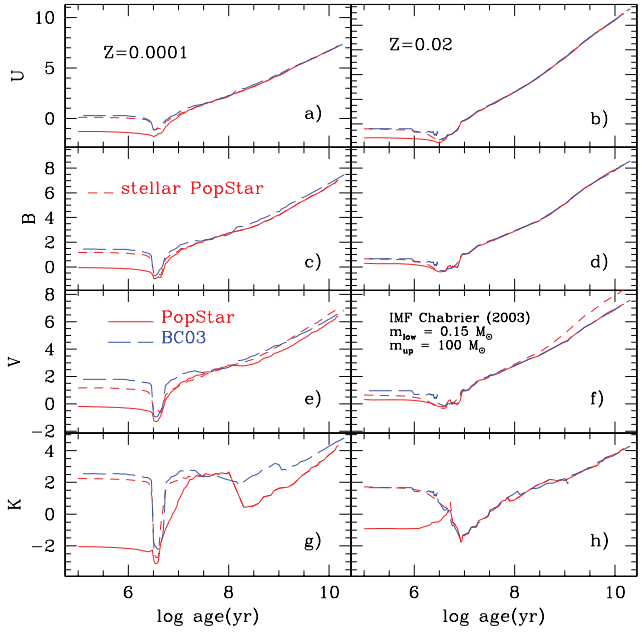

Figure 25. Magnitude evolution in *U*, *B*, *V* and *K* with the age obtained in this work compared with the corresponding ones from GALAXEV. Solid red lines are PopStar models, while the dashed blue lines are those models from GALAXEV. Dashed red lines are the results obtained for the stellar PopStar models without the nebular contribution.

4.3 Comparison of results with GALAXEV models

Here we compare our results with GALAXEV models (BC03) that are particularly well suited for old populations. Fig. 25 shows the comparison of the *U*, *B*, *V* and *K* magnitudes, while Fig. 26 shows the comparison of $U-B$, $B-V$, $V-R$, $V-I$ and $V-K$ colours. For all models, we have assumed a Chabrier IMF with solid red lines indicating our PopStar models and dashed blue lines depicting

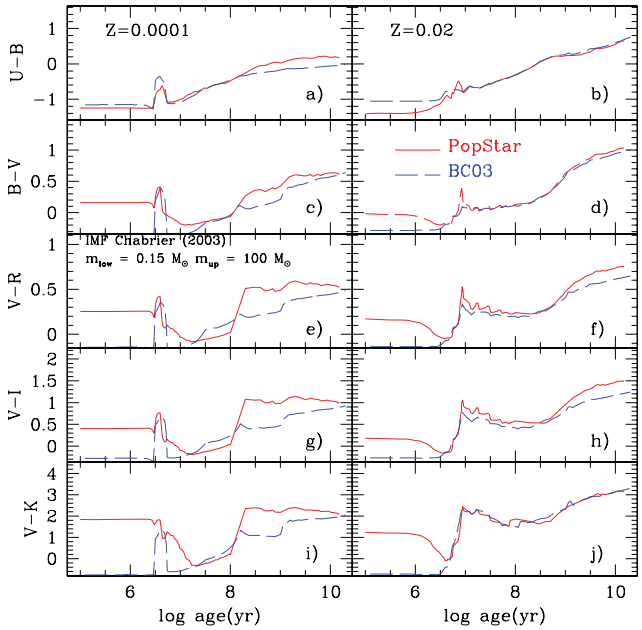

Figure 26. Colour evolution: $U-B$, $B-V$, $V-R$, $V-I$ and $V-K$ colours obtained for PopStar compared with the corresponding ones from GALAXEV. The same coding line from the previous figures has been used.

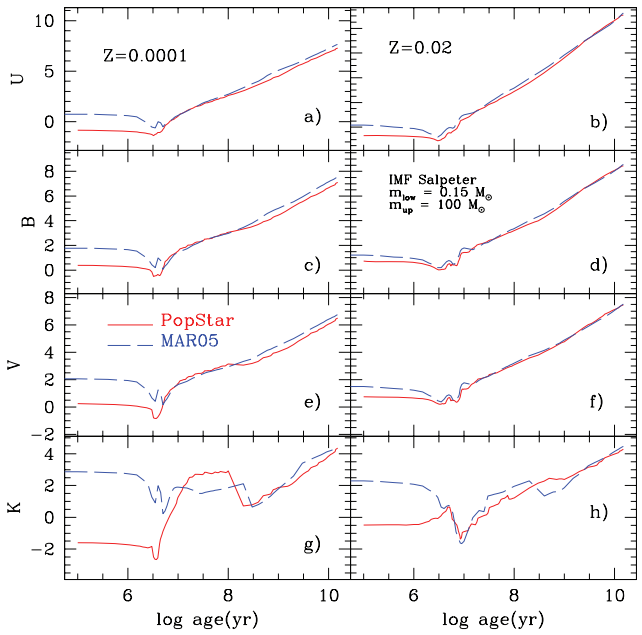

Figure 27. Magnitude evolution in bands U, B, V and K for PopStar, compared to the corresponding ones from MAR05 with the same coding line from the previous figures as labelled in the plot.

the corresponding GALAXEV models. Left-hand panels show the evolution for $Z = 0.0001$, while right-hand panels refer to $Z = 0.02$. At young ages, our colours are significantly redder than those of BC03, mainly because BC03 do not include the effects of nebular continuum. To show this, we plot in Fig. 25 as short-dashed red lines the results obtained for the PopStar stellar spectra without the continuum nebular contribution. The results are very similar to those from BC03. The difference PopStar–BC03 increases at decreasing metallicity because the strength of the nebular emission increases at decreasing metallicity. As already said, including this contribution at young ages produces a reddening of the $V-K$ colours from 2 to 3 mag, depending on the initial metallicity. This contribution is thus relevant and should be included in the interpretation of the spectral evolution of star-forming galaxies. At intermediate and old ages, the differences in magnitudes and in colours are small, in particular for the case of solar metallicity. At low metallicity, the difference becomes larger, especially in the $V-K$. The origin of this difference is most likely a different algorithm to describe the mass-loss rates. This can be seen also from Fig. 29, where we perform a comparison of the spectral evolution of a solar metallicity SSP, predicted by different authors. We note that, contrary to the other models, a significant P-AGB phase is already present after 100 Myr in our models. From the same figure, we may also note the effects of the inclusion of the new spectra of PNe. Both effects combine to produce a P-AGB phase with a lower far-UV luminosity.

4.4 Comparison of results with Maraston models

We have also compared our PopStar results with MAR05 models. The evolution of selected magnitudes and colours is shown in Figs 27 and 28, respectively. We have used the same symbols and line coding used in the previous figures.

Since MAR05 does not include nebular emission, a large difference is present at very young ages, as before. There are also differences at older ages which may reach a magnitude in the

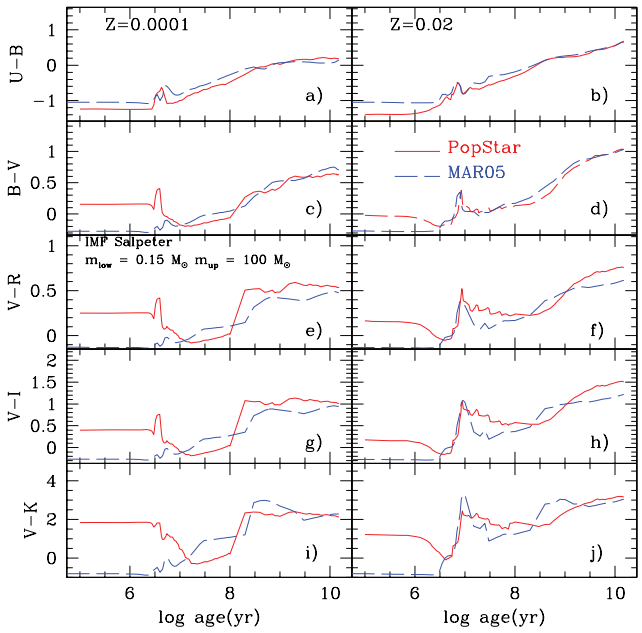

Figure 28. Colour evolution showing $U-B$, $B-V$, $V-R$, $V-I$ and $V-K$ with age obtained in this work compared with the corresponding ones from MAR05 with the same coding line from the previous figures.

$V-K$ colour. The differences with respect to MAR05 models are, in general, larger than those with respect to BC03 models.

Finally, Fig. 29 shows the comparison of the spectral evolution computed with PopStar for an SSP with solar metallicity and an SAL2 IMF with other codes existing in the literature, Leitherer et al. (1999) named as STB99, Bruzual & Charlot (2003) as BC03, Maraston (2005) as MAR05, González Delgado et al. (2005) as GON05 and with our old models, Mollá & García-Vargas (2000) as MGV00, at some selected ages, as given in each panel.

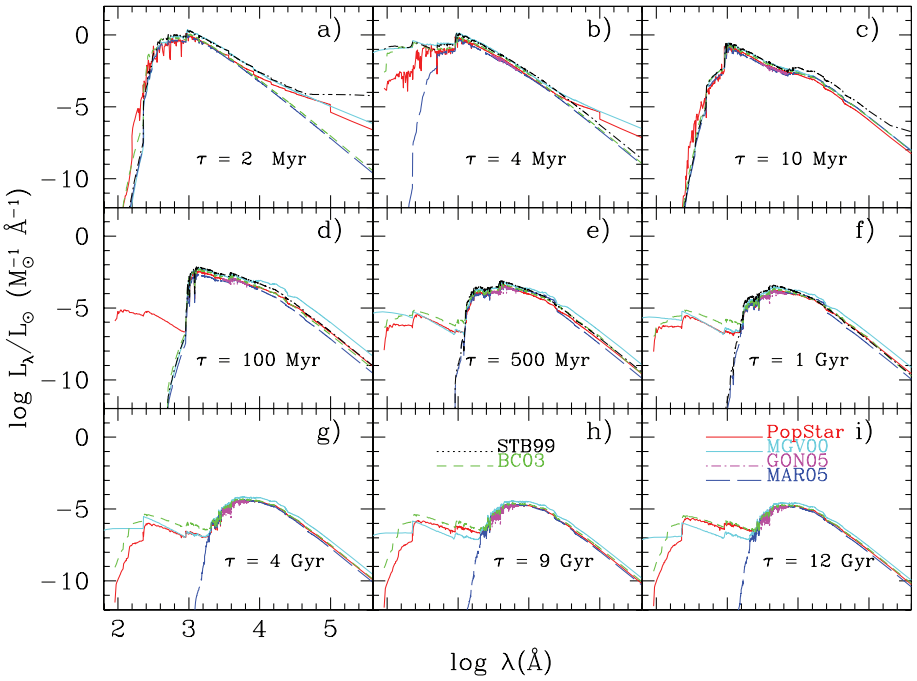

Figure 29. SEDs comparison. Our models, PopStar, are plotted together with those from MGV00, GON05, MAR05, STB99 and GALAXEV (BC03). Each model is represented by a different line. Different ages sampling the whole evolution are plotted.

From this figure, it appears that MAR05 models lack both the hard ionizing flux of the WR stars as well as that of P-AGB stars. On the other hand, STB99 models lack the P-AGB phase. GON05 models were calculated with higher resolution but within a shorter wavelength range (from 3000 to 7000 Å) than the other models. The only models that include the hard ionizing flux of WR stars and that of P-AGB stars are those by BC03 and our old and new ones.

Our new models are similar to our old MGV models. However, the different procedure of temperature assignation and the different spectral library adopted, in the WR phase, result in a significantly less hard ionizing spectrum This effect is also present in the P-AGB phase. The nebular continuum is now more accurate because it includes not only the hydrogen but also the helium contribution. Furthermore, in the common wavelength range, our new models compare very well also with GON05 models.

From Fig. 29, we see that our models reproduce the behaviour of the STB99 models at young ages very well. Moreover, PopStar models follow the evolution of the GALAXEV and MAR05 models at old ages very well. Thus, since STB99 models were specifically calibrated for starburst galaxies, while GALAXEV and MAR05 were mainly calibrated for intermediate/old ages, we conclude that PopStar models can be safely used over the whole age range of stellar populations.

5 CONCLUSIONS

We have computed new synthesis models that follow the evolution of SSPs from very young to very old ages. To this purpose, we have combined the homogeneous and well-calibrated set of Padova 94 stellar evolution models, with the most recent physics input concerning stellar atmospheres and, where needed, nebular continuum emission. Besides spectra over a wide wavelength range, these models provide a large quantity of additional information, useful for the analysis of the properties of stellar populations (see Appendix A).

From the comparison of our models with previous evolutionary synthesis models, we have shown that our models are well calibrated and can be safely applied over the whole age range of stellar populations. This is particularly important because we have shown that not all existing models include all the relevant evolutionary phases of stellar populations

For this reason, our models are particularly suited for the study of galaxies where a combination of stellar populations of different ages and metallicities coexist.

Our new models, the resulting SEDs and HR diagrams are available in the Virtual Observatory (models in http://esavo.esa.int/vospec/ and the PopStar web page at http://www.fractal-es.com/SEDmod.htm).

ACKNOWLEDGMENTS

This work has been partially supported by DGICYT grant AYA2007–67965-C03-03 and by the Spanish MEC under the Consolider-Ingenio 2010 Programme grant CSD2006-00070: First Science with the GTC (http://www.iac.es/consolider-ingenio-gtc/). AB acknowledges contract ASI-INAF I/016/07/0.

REFERENCES

Aller L. H., 1991, in Lawrence H. Aller, ed., Atoms, Stars, and Nebulae. Cambridge Univ. Press, Cambridge, p. 380
Annibali F., Bressan A., Rampazzo R., Zeilinger W. W., Danese L., 2007, A&A, 463, 455
Asari N. V., Cid Fernandes R., Stasińska G., Torres-Papaqui J. P., Mateus A., Sodré L., Schoenell W., Gomes J. M., 2007, MNRAS, 381, 263
Bicker J., Fritze-v.Alvensleben U., Möller C. S., Fricke K. J., 2004, A&A, 413, 37
Bressan A. G., Chiosi C., Bertelli G., 1984, A&A, 130, 279
Bressan A., Fagotto F., Bertelli G., Chiosi C. 1993, A&AS, 100, 647
Bressan A., Chiosi C., Fagotto F., 1994, ApJS, 94, 63
Bressan A., Granato G. L., Silva L., 1998, A&A, 332, 135

Bressan A., Silva L., Granato G. L., 2002, A&A, 392, 377
Bressan A. et al., 2006, ApJ, 639, L55
Brown R. L., Mathews W. G., 1970, ApJ, 160, 939
Bruzual A. G., 2007, in Vazdekis A., Peletier R. F., eds, IAU Symp. 241, Stellar Populations as Building Blocks of Galaxies. Cambridge Univ. Press, Cambridge, p. 125
Bruzual A. G., 1983, ApJ, 273, 105
Bruzual G., Charlot S., 2003, MNRAS, 344, 1000 (BC03)
Carraro G., Girardi L., Bressan A., Chiosi C., 1996, A&A, 305, 849
Castor J., McCray R., Weaver R., 1975, ApJ, 200, L107
Cerviño M., Luridiana V., 2004, A&A, 413, 145
Cerviño M., Luridiana V., 2006, A&A, 451, 475
Cerviño M., Valls-Gabaud D., Luridiana V., Mas-Hesse J. M., 2002, A&A, 381, 51
Cerviño M., Luridiana V., Jamet L., 2008, A&A, 491, 693
Chabrier G., 2003, ApJ, 586, L133
Chavez M. et al., 2009, ApJ, in press (arXiv:0905.3496)
Chiosi C., Bertelli G., Bressan A., 1988, A&A, 196, 84
Cid Fernandes R., Asari N. V., Sodré L., Stasińska G., Mateus A., Torres-Papaqui J. P., Schoenell W., 2007, MNRAS, 375, L16
Clemens M. S., Bressan A., Nikolic B., Alexander P., Annibali F., Rampazzo R., 2006, MNRAS, 370, 702
Clemens M. S., Bressan A., Nikolic B., Rampazzo R., 2009a, MNRAS, 392, L35
Clemens M. S., Bressan A., Panuzzo P., Rampazzo R., Silva L., Buson L., Granato G. L., 2009b, MNRAS, 392, 982
Coelho P., Bruzual G., Charlot S., Weiss A., Barbuy B., Ferguson J. W., 2007, MNRAS, 382, 498
Ercolano B., Storey P. J., 2006, MNRAS, 372, 1875
Fagotto F., Bressan A., Bertelli G., Chiosi C., 1994a, A&AS, 105, 29
Fagotto F., Bressan A., Bertelli G., Chiosi C., 1994b, A&AS, 104, 365
Ferland G. J., 1980, PASP, 92, 596
Ferland G. J., Korista K. T., Verner D. A., Ferguson J. W., Kingdon J. B., Verner E. M., 1998, PASP, 110, 761
Ferrini F., Penco U., Palla F., 1990, A&A, 231, 391
Fritze-v.Alvensleben U., Bicker J., 2006, A&A, 454, 67
García-Vargas M. L., Díaz A. I., 1994, ApJS, 91, 553
García-Vargas M. L., Bressan A., Díaz A. I., 1995, ApJS, 112, 35
García-Vargas M. L., Mollá M., Bressan A., 1998, A&A, 130, 513
Girardi L., Bressan A., Chiosi C., Bertelli G., Nasi E., 1996, A&AS, 117, 113
Girardi L., Bertelli G., Bressan A., Chiosi C., Groenewegen M. A. T., Marigo P., Salasnich B., Weiss A., 2002, A&A, 391, 195
Girardi L., Grebel E. K., Odenkirchen M., Chiosi C., 2004, A&A, 422, 205
González Delgado R. M., Cerviño M., Martins L. P., Leitherer C., Hauschildt P. H., 2005, MNRAS, 357, 945 (GON05)
Goudfrooij P., Gilmore D., Kissler-Patig M., Maraston C., 2006, MNRAS, 369, 697
Hillier D. J., Miller D. L., 1998, ApJ, 496, 407
Kroupa P., 2001, MNRAS, 322, 231
Kyeong J.-M., Tseng M.-J., Byun Y.-I., 2003, A&A, 409, 479
Leitherer C. et al., 1999, ApJS, 123, 3 (STB99)
Lejeune T., Cuisinier F., Buser R., 1997, A&AS, 125, 229
Maraston C., 2005, MNRAS, 362, 799 (MAR05)
Marigo P., Girardi L., Bressan A., Groenewegen M. A. T., Silva L., Granato G. L., 2008, A&A, 482, 883
Meynet G., Maeder A., 2005, A&A, 429, 581
Mollá M., García-Vargas M. L., 2000, A&A, 359, 18 (MGV00)
Nussbaumer H., Schmutz W., 1984, A&A, 138, 495
Osterbrock D. E., 1989, Astrophysics of Gaseous Nebulae and Active Galactic Nuclei. Univ. Sci. Books, Mill Valley, CA
Panuzzo P., Bressan A., Granato G. L., Silva L., Danese L., 2003, A&A, 409, 99
Pauldrach A. W. A., Hoffmann T. L., Lennon M., 2001, A&A, 375, 161
Persson S. E., Aaronson M., Cohen J. G., Frogel J. A., Matthews K., 1983, ApJ, 266, 105
Pessev P. M., Goudfrooij P., Puzia T. H., Chandar R., 2006, AJ, 132, 781
Rauch T., 2003, A&A, 403, 709
Salpeter E. E., 1955, ApJ, 121, 161
Silva L., Granato G. L., Bressan A., Danese L., 1998, ApJ, 509, 103
Smith L. J., Norris R. P. F., Crowther P. A., 2002a, MNRAS, 337, 1309
Smith J. A. et al., 2002b, AJ, 123, 2121
Tinsley B. M., 1972, A&A, 20, 383
Úbeda L., Maíz-Apellániz J., MacKenty J. W., 2007, AJ, 133, 917
Vanbeveren D., Van Bever J., Belkus H., 2007, ApJ, 662, L107
van Loon J. T., Boyer M. L., McDonald I., 2008, ApJ, 680, L49
Vázquez G. A., Leitherer C., Schaerer D., Meynet G., Maeder A., 2007, ApJ, 663, 995
Vega O., Clemens M. S., Bressan A., Granato G. L., Silva L., Panuzzo P., 2008, A&A, 484, 631
Walborn N. R., Maíz-Apellániz J., Barbá R. H., 2002, AJ, 124, 1601

APPENDIX A: PRODUCTS AVAILABLE

The resulting SEDs are available in the VO (models in http://esavo.esa.int/vospec/ and both SEDs and HR diagrams are also available at http://www.fractal-es.com/SEDmod.htm).

The products already available in the PopStar webpage described in this paper are (1) SSP models for different IMF parameters, ages and metallicities; (2) HR diagrams for different IMF parameters, ages and metallicities; (3) result tables with SSP's properties related to the cluster ionization power: numbers of O, B, WN, WC, WO, SN, PN, ionizing photons [Q(H), Q(He), Q[He^+, Q(O)], etc.]. Other available products in the web page are the emission line spectra of the ionized gas resulting from the ionizing clusters (described in Paper II) and the photometrical parameters, in which the colours have been computed taking into account the contribution of the emission line spectra for the youngest ages. The photometrical results are presented and discussed in Paper III.

(i) *HR diagrams*.

(a) $M/M_\odot$-HR = initial mass ($M_\odot$).

(b) $T_{\rm eff}$-HR = effective temperature (K) as computed in the isochrone.

(c) log$g$-HR = logarithm of the gravity (cm s^{-2}) from the isochrone.

(d) log($L/L_\odot$)-HR = logarithm of the luminosity (in $L_\odot$), from the isochrone.

(e) $T_{\rm eff}$-Mod = effective temperature (K) as computed of the assigned model.

(f) log$g$-Mod = logarithm of the gravity (cm s^{-2}).

(g) log($L/L_\odot$)-Mod = logarithm of the luminosity (in $L_\odot$);

(h) log($M\dot{M}$) = logarithm of the mass loss (in $M_\odot$ yr^{-1}).

(i) Err($T_{\rm eff}$) = error associated with the $T_{\rm eff}$ (K) assignation.

(j) Err(log$L/L_\odot$) = error associated with the log($L/L_\odot$) assignation.

(k) WR = parameter with the following meaning: 1 (WN star), 2 (WC star), 3 (evolved hot star, e.g. PN), 0 NS (all the stars non-included in the previous categories).

(l) $n_{\rm star-sal1}$ = number of stars in that mass interval (weights) with IMF-1 normalized to 1 $M_\odot$ cluster.

(m) $n_{\rm star-sal2}$ = number of stars in that mass interval (weights) with IMF-2 normalized to 1 $M_\odot$ cluster.

(n) $n_{\rm star-fer}$ = number of stars in that mass interval (weights) with IMF-3 normalized to 1 $M_\odot$ cluster.

(o) $n_{\rm star-kro}$ = number of stars in that mass interval (weights) with IMF-4 normalized to 1 $M_\odot$ cluster.

(p) $n_{\rm star-cha}$ = number of stars in that mass interval (weights) with IMF-5 normalized to 1 $M_\odot$ cluster.

(ii) *SEDs*: we provide the spectra (SEDs) normalized to 1 $M_\odot$ cluster. Each file has four columns with the following contents.

(a) λ (Å) = wavelength.
(b) $L_{star_\lambda}/L_\odot$ (Å^{-1}) = star continuum.
(c) $L_{neb_\lambda}/L_\odot$ (Å^{-1}) = nebular continuum.
(d) $L_{tot_\lambda}/L_\odot$ (Å^{-1}) = total (star+nebular) continuum.

Spectra can be chosen by IMF type, age and metallicity. All the spectra have been normalized to a total mass of 1 $M_\odot$. To convert the luminosities in erg s^{-1}, you need to multiply by the solar luminosity, $L_\odot = 3.82 \times 10^{33}$ erg s^{-1}. Spectra can be managed with VOSPEC.

(iii) *Parameters relevant to the ionization cluster power*: we provide three tables with the following information (all the numbers have been normalized to 1 $M_\odot$).

(a) log(Age) = logarithm of the age (in years).
(b) N_{tot} = total number of stars at the time of cluster formation.
(c) N_{20} = total number of stars with $M \leq 20\,M_\odot$.
(d) N_{OB} = total number of O, B stars present at the current age.
(e) N_{WN} = total number of WN stars present at the current age.
(f) N_{WC} = total number of WC stars present at the current age.
(g) N_{RSG} = total number of RSG stars present at the current age.
(h) N_{SN} = total number of SNe Ib+II exploded in each age step.
(i) N_{PN} = total number of PN present at the current age.
(j) E_{winds} = total mechanical energy deposited by winds at the current age.
(k) E_{SNe} = total mechanical energy deposited by SNe in each age step.
(l) R_c = cluster radius at the current age (from mechanical energy deposition due to winds+SNe).
(m) $Q(H)$ = total number of H I ionizing photons, $Q(H)$, $\lambda <$ 912.4 Å in s^{-1}.
(n) $Q(He)$ = total number of He I ionizing photons, $Q(He)$, $\lambda <$ 504.6 Å in s^{-1}.
(o) $Q(O)$ = total number of O I ionizing photons, $Q(O)$, $\lambda <$ 353.3 Å in s^{-1}.
(p) $Q(He^+)$ = total number of He II ionizing photons, $Q(He^+)$, $\lambda <$ 228.0 Å in s^{-1}.

SUPPORTING INFORMATION

Additional Supporting Information may be found in the online version of this article:

Table 2: Number of stars of different type in each age.
Table 4: Mechanical energy injected into the ISM.
Table 5: The number of ionizing photons.
Table 7: Hβ and Hα emission and absorption line luminosity, continuum luminosity and equivalent widths, in emission, in absorption and total.
Table 8: Example of the evolution of the magnitudes in the Johnson–Cousins–Glass photometric system.
Table 9: SDSS magnitudes.
Figure 5: Additional panels corresponding to $Z = 0.05$, 0.008, 0.004, 0.0004 and 0.0001, respectively.
Figure 6: Upper panel: effective temperature assigned to each star as a function of the corresponding T_{eff} in the isochrome, for solar abundance as labelled. Bottom panel: same comparison for stellar gravity values.
Figure 7: Assignation error, in percentage, in the effective temperature for solar abundance: (a) NS as a function of their masses and (b) P-AGB stars (PN), as a function of T_{eff}.

Please note: Wiley-Blackwell are not responsible for the content or functionality of any supporting information supplied by the authors. Any queries (other than missing material) should be directed to the corresponding author for the article.

This paper has been typeset from a TEX/LATEX file prepared by the author.